SPITZER Mid-IR Spectroscopy of Powerful 2Jy and 3CRR Radio Galaxies. II. AGN Power Indicators and Unification

The Astrophysical Journal, 788:98 (22pp), 2014 June 20 doi:10.1088/0004-637X/788/2/98

SPITZER MID-IR SPECTROSCOPY OF POWERFUL 2Jy AND 3CRR RADIO GALAXIES. II. AGN POWER INDICATORS AND UNIFICATION

D. Dicken[1], C. Tadhunter[2], R. Morganti[3,4], D. Axon[5,6,17], A. Robinson[5], M. Magagnoli[5], P. Kharb[7], C. Ramos Almeida[8,9], B. Mingo[10], M. Hardcastle[11], N. P. H. Nesvadba[12], V. Singh[12], M. B. N. Kouwenhoven[13], M. Rose[14], H. Spoon[14], K. J. Inskip[15], and J. Holt[16]
[1] CEA-Saclay, F-91191 Gif-sur-Yvette, France; daniel.dicken@cea.fr
[2] University of Sheffield, Hounsfield Road, Sheffield S3 7RH, UK
[3] ASTRON, P.O. Box 2, 7990 AA Dwingeloo, The Netherlands
[4] Kapetyn Astronmical Institute, University of Groningen, Postbuss 800, 9700 AV Groningen, The Netherlands
[5] Rochester Institute of Technology, 84 Lomb Memorial Drive, Rochester, NY 14623, USA
[6] University of Sussex, Pevensey 2, University of Sussex, Falmer, Brighton BN1 9QH, UK
[7] Indian Institute of Astrophysics, II Block, Koramangala, Bangalore 560034, India
[8] Instituto de Astrofisica de Canarias (IAC), C/V ia Lactea, s/n, E-38205 La Laguna, Tenerife, Spain
[9] Departamento de Astrofisica, Universidad de La Laguna, E-38205 La Laguna, Tenerife, Spain
[10] Department of Physics & Astronomy, University of Leicester, University Road, Leicester LE1 7RH, UK
[11] School of Physics, Astronomy and Mathematics, University of Hertfordshire, College Lane, Hatfield AL10 9AB, UK
[12] Institut d'Astrophysique Spatiale, CNRS, Université Paris Sud, F-91405 Orsay, France
[13] Kavli Institute for Astronomy and Astrophysics, Peking University, Yi He Yuan Lu 5, Haidian Qu, Beijing 100871, China
[14] 224 Space Sciences Building, Cornell University, Ithaca, NY 14853, USA
[15] Max Planck Institute for Astronomy, Königstuhl 17, D-69117 Heidelberg, Germany
[16] Leiden Observatory, Leiden University, P.O. Box 9513, 2300 RA Leiden, The Netherlands
Received 2013 November 4; accepted 2014 March 11; published 2014 May 28

ABSTRACT

It remains uncertain which continuum and emission line diagnostics best indicate the bolometric powers of active galactic nuclei (AGNs), especially given the attenuation caused by the circumnuclear material and the possible contamination by components related to star formation. Here we use mid-IR spectra along with multiwavelength data to investigate the merit of various diagnostics of AGN radiative power, including the mid-IR [Ne III] λ25.89 μm and [O IV] λ25.89 μm fine-structure lines, the optical [O III] λ5007 forbidden line, and mid-IR 24 μm, 5 GHz radio, and X-ray continuum emission, for complete samples of 46 2Jy radio galaxies ($0.05 < z < 0.7$) and 17 3CRR FRII radio galaxies ($z < 0.1$). We find that the mid-IR [O IV] line is the most reliable indicator of AGN power for powerful radio-loud AGNs. By assuming that the [O IV] is emitted isotropically, and comparing the [O III] and 24 μm luminosities of the broad- and narrow-line AGNs in our samples at fixed [O IV] luminosity, we show that the [O III] and 24 μm emission are both mildly attenuated in the narrow-line compared to the broad-line objects by a factor of $\approx$2. However, despite this attenuation, the [O III] and 24 μm luminosities are better AGN power indicators for our sample than either the 5 GHz radio or the X-ray continuum luminosities. We also detect the mid-IR 9.7 μm silicate feature in the spectra of many objects but not ubiquitously: at least 40% of the sample shows no clear evidence for these features. We conclude that, for the majority of powerful radio galaxies, the mid-IR lines are powered by AGN photoionization.

Key words: galaxies: active – infrared: galaxies

Online-only material: color figures, extended figure

1. INTRODUCTION

Orientation-based unified schemes propose that certain components of the emission from active galactic nuclei (AGNs) are radiated anisotropically (e.g., Urry & Padovani 1995). It is widely believed that part of this orientation dependence is caused by obscuring dust structures in the shape of tori or warped disks around the central AGN and broad-line regions (e.g., Antonucci 1984; Nenkova et al. 2008; Lawrence & Elvis 2010). This implies that, although AGNs may have a common central engine, they can look drastically different in terms of their emission line spectra and broadband continuum emission, as the orientation changes with respect to the line of sight.

While the concept of obscuration-induced anisotropy is useful for our understanding of the relationship between type 1 and type 2 AGNs, the obscuring dust and gas can hinder our ability to determine key intrinsic properties of AGNs such as their total radiative (bolometric) powers. In particular, the degree to which different optical emission components suffer from obscuration is uncertain. Therefore, it is important to identify alternative bolometric AGN power indicators that do not suffer from attenuation. This is necessary both to further test unification ideas and to improve our understanding of the AGN population as a whole (e.g., Singh et al. 2011). Radio-loud AGNs are popular candidates for unbiased studies of AGNs because they can be selected using their low-frequency extended radio lobe emission, which is known to be emitted isotropically and is linked to the central AGN via the relativistic jets. Numerous studies have used radio-selected samples to probe the orientation dependence of AGNs and test the orientation-based unified schemes (e.g., Jackson & Browne 1990; Hes et al. 1995; Haas et al. 2005).

We have been engaged in a major multiwavelength study of a complete sample of radio-selected, southern, 2Jy radio galaxies. In our previous work (Dicken et al. 2009, 2010) we investigated AGN power indicators in our samples and showed

[17] Deceased 5 April 2012.

that [O III] optical emission line luminosity ($L_{[O\,III]}$) is strongly correlated with both the mid-IR (24 μm) and far-IR (70 μm) continuum luminosities ($L_{24\,\mu m}$ and $L_{70\,\mu m}$, respectively). $L_{[O\,III]}$ is a potentially useful AGN power indicator because it is emitted far from the broad-line AGN nucleus (including the accretion disk component) and is therefore less likely to be affected by the obscuration due to dust structures in the near-nuclear regions (Tadhunter et al. 1998; Simpson 1998). Therefore, the correlations between $L_{24\,\mu m}$, $L_{70\,\mu m}$, and $L_{[O\,III]}$ provide strong empirical evidence to support AGN illumination as the dominant heating mechanism for the thermal, mid- to far-IR (MFIR) emitting dust in powerful radio galaxies. However, this result is dependent on the reliability of $L_{[O\,III]}$ as an AGN power indicator, in particular, whether the [O III] line suffers some dust obscuration by the outer parts of the torus or larger-scale dust structures in the host galaxies (e.g., Jackson & Browne 1990; Simpson 1998; Baldi et al. 2013).

In addition, although the mid-IR continuum (15–30 μm) emission is often assumed to be isotropic in nature and therefore a good candidate for an AGN power indicator, there is some evidence in previous *Spitzer* and *Wide-field Infrared Survey Explorer* investigations that obscuration could also affect the photometric flux measurements at mid-IR wavelengths (24 μm) in radio galaxies (e.g., Cleary et al. 2007; Leipski et al. 2010; Gurkan et al. 2013). Moreover, the strong possibility of a starburst contribution rules out the longer-wavelength, far-IR, continuum luminosities as reliable AGN power proxies (Dicken et al. 2009, 2012).

We further note that, although the low-frequency radio emission is almost certainly isotropically emitted, the use of radio emission as an AGN power indicator has some notable drawbacks (Dicken et al. 2008). In particular, because the radio emission is emitted by lobes on large scales (up to hundreds of kiloparsecs), it represents the jet power integrated over timescales of $\approx 10^6$ yr (e.g., Tadhunter et al. 2012). Moreover, the radio jet power is not necessarily closely coupled with AGN radiative power because the amount of accretion energy converted into jet power may depend on parameters such as the spin of the supermassive black hole (e.g., Blandford & Znajek 1977; Punsly & Coroniti 1990). In addition, radio luminosities are also potentially dependent on the gaseous environments with which the jets are interacting (Barthel & Arnaud 1996), introducing variations in radio luminosities for otherwise identical intrinsic jet/AGN powers (Ramos Almeida et al. 2013; Hardcastle & Krause 2013).

Finally, although the X-ray continuum luminosity has the advantage that it is unequivocally linked to the AGN, because of its origin in the corona of the accretion disk, it suffers from the most variability compared to the other AGN power indicators. This is because it is emitted on the smallest scales, closest to the AGN, and therefore closely follows the instantaneous AGN power. In contrast, larger-scale emission components (e.g., the narrow-line region) integrate the AGN power over longer timescales. Furthermore, careful modeling of the X-ray observations is required to account for the effects of absorption and beamed nonthermal emission on the measured continuum fluxes (e.g., Hardcastle et al. 2009).

Clearly, all the AGN power indicators have potential drawbacks. Therefore, it is important to investigate their relative usefulness using complete samples of AGNs with comprehensive multiwavelength data sets.

This paper is the second in a series that analyzes data from the *Spitzer* Infrared Spectrograph (IRS; Houck et al. 2004; program 50588, PI: Tadhunter). The mid-IR spectral lines contained in these data provide important information about the degree of anisotropy and hence utility of various AGN power indicators. For example, [O IV] λ25.89 μm has a relatively high ionization potential (E_{ion} = 54.9 eV), which favors an AGN origin; it also lies at the longer wavelength end of the IRS window and so is least likely to suffer from the effects of attenuation by the circumnuclear interstellar medium (ISM). Indeed, several *Spitzer* spectroscopic studies have identified [O IV] λ25.89 μm as a good candidate for an isotropic tracer of AGN power in samples of Seyfert galaxies (e.g., Diamond-Stanic et al. 2009; LaMassa et al. 2010).

Mid-IR spectral studies can also allow tests of the orientation-based unified schemes for AGNs using measurements of the broad silicate features detected in absorption in some AGNs and, relatively recently, also detected in emission in others (Siebenmorgen et al. 2005; Hao et al. 2005). Amorphous silicate grains have strong opacity peaks due to the Si–O stretching and the O–Si–O bending modes, leading to features at 9.7 and 18 μm in the mid-IR spectrum. In a simple interpretation of the unified schemes, and as predicted by the theoretical work of Nenkova et al. (2002, 2008), one may expect to detect silicate emission in AGNs classified as broad-line objects at optical wavelengths in which circumnuclear dust emission is relatively unattenuated. On the other hand, silicate absorption is likely to be associated with AGNs classified as narrow-line objects at optical wavelengths because of the attenuation of the mid-IR continuum by columns of dust along the line of sight. Many previous AGN studies have found this premise to hold in *general* terms (e.g., Shi et al. 2006; Hao et al. 2007; Gallimore et al. 2010; Landt et al. 2010). However, it is important to note that evidence for silicate emission has been detected in narrow-line quasars (Sturm et al. 2006; Nikutta et al. 2009) and type 2 Seyferts (Mason et al. 2009), which is explained in theoretical models by directly illuminated dust within a clumpy torus (Nenkova et al. 2008).

In the first paper of the series (Dicken et al. 2012) we presented the spectra and a detailed description of the data analysis methodology and also investigated the star formation properties of the samples. In this second paper we analyze the mid-IR emission line properties of the IRS spectra, focusing the study on diagnostics of AGN power, as well as testing the unified schemes for radio-loud AGNs. We assume a cosmology with $H_o = 71\,\mathrm{km\,s^{-1}\,Mpc^{-1}}$, $\Omega_m = 0.27$, and $\Omega_\lambda = 0.73$ throughout this paper.

2. SAMPLES AND SELECTION

The 2Jy sample presented in this work is identical to that presented in our previous papers relating to the *Spitzer Space Telescope* observations of powerful southern radio galaxies (Tadhunter et al. 2007; Dicken et al. 2008, 2009, 2010, 2012). It consists of all 46 powerful radio galaxies and steep-spectrum quasars ($F_\nu \propto \nu^{-\alpha}$, $\alpha_{2.7}^{4.8} > 0.5$) selected from the 2Jy sample of Wall & Peacock (1985) with redshifts $0.05 < z < 0.7$, flux densities $S_{2.7\,GHz} > 2$Jy and declinations $\delta < 10^\circ$. The spectral index cut has been set to ensure that all the sources in the sample are dominated by steep-spectrum lobe emission, while the lower redshift limit has been set to ensure that these galaxies are genuinely powerful radio sources.

The mid-IR spectra analyzed in this paper complement a wealth of data that has been obtained for the 2Jy sample over the last two decades. To date, these include deep optical spectroscopic observations (Tadhunter et al. 1993, 1998, 2002; Wills

et al. 2002; Holt et al. 2007), extensive observations at radio wavelengths (Morganti et al. 1993, 1997, 1999; Dicken et al. 2008), complete deep optical imaging from Gemini (Ramos Almeida et al. 2011, 2012), and deep Multiband Imaging Photometer for *Spitzer* (MIPS) and *Herschel* Photodetector Array Camera and Spectrometer (PACS) MFIR photometric observations (Dicken et al. 2008; D. Dicken et al. 2014, in preparation; detection rates of 100%, 90%, 100%, and 90% at 24, 70, 100, and 160 μm, respectively). In addition, 98% of the complete sample has recently been observed at X-ray wavelengths with *XMM* and *Chandra* (Mingo et al. 2013), and 78% of the sample has deep 2.2 μm (*K*-band) near-infrared imaging (Inskip et al. 2010).

A major advantage of our full sample of 46 objects is that it includes a range of optical broad-line radio galaxies and radio-loud quasars (BLRG/Q: 35%), narrow-line radio galaxies (NLRG: 43%), and weak-line radio galaxies[18] (WLRG: 22%). In terms of radio morphological classification, the sample includes 72% FRII sources, 13% FRI sources, and 15% compact steep spectrum (CSS)/gigahertz peak spectrum (GPS) objects. The sample is presented in Table 1.[19]

We also present the results for a complete subsample of 17 3CRR radio-loud AGNs[20] selected from the sample of Laing et al. (1983). We have limited this sample to objects with FRII radio morphologies and redshifts $z \leqslant 0.1$, leading to a sample that is complete in both *Spitzer*/MIPS detections (100% at 24 μm and 89% at 70 μm) and [O III] λ5007 emission line flux measurements (100%). The full sample of 17 objects also includes a range of BLRG/Q (12%), NLRG (53%), and WLRG (35%) class objects. Because the 3CRR objects have lower radio powers and redshifts on average than most of the 2Jy sample, they help add statistical significance to the lower-luminosity end of the 2Jy sample in our investigations (see Dicken et al. 2012 for more details). Throughout the rest of this paper we will refer to this sample as the 3CRR sample. In addition, when discussing the investigation of the 2Jy and 3CRR sample objects together, we will refer to this as the combined sample.

2.1. Data Processing

The mid-IR spectra of 35 out of the 46 objects in the 2Jy sample were obtained in a dedicated campaign of *Spitzer* IRS observations (program 50558; PI: Tadhunter) between 2008 July and 2009 March and were first published in Dicken et al. (2012). The spectra of 8 additional objects in the 2Jy sample and the 15 objects from the 3CRR sample were obtained from the *Spitzer* archive and were observed between 2004 August and 2006 September. These data came from various campaigns under several different PIs and, consequently, have varying integration times and observing modes. Note that some of the latter data were first published in previous papers (e.g., Ogle et al. 2006; Leipski et al. 2009).

[18] WLRG are defined as having low [O III] emission line equivalent widths: EW([O III]) < 10 Å (Tadhunter et al. 1998). WLRG are also sometimes referred to as low-excitation radio galaxies (LERG) in the literature (see Buttiglione et al. 2009 for discussion).

[19] Additional information on the 2Jy sample can be found at http://2jy.extragalactic.info.

[20] In Dicken et al. (2012) we stated that the 3CRR sample comprised 19 objects and that 2 objects overlap between the 3CRR and 2Jy samples (3C403 and 3C445). However, in fact, the latter two objects are drawn from the 3CR sample, rather than the 3CRR sample of Laing et al. (1983). Because both of these objects are already in the 2Jy sample and we do not consider the 2Jy and 3CRR samples separately in our analysis, none of our results are affected if we omit the two objects from the 3CRR sample.

Out of the 46 objects in the 2Jy sample, 43 (93%) were successfully observed and detected by *Spitzer*/IRS. For the 17 3CRR sample objects 13 (76%) were successfully observed and detected. The fully reduced rest frame spectra for the 43 observed/detected objects in the 2Jy sample and the 13 objects from the 3CRR sample are presented in Dicken et al. (2012) and are included here in an Appendix in the online journal. Dicken et al. (2012) also present a detailed description of the observations and the data reduction methodology, which includes the use of the SMART (v.8.1.2.) program, developed by the IRS Team at Cornell University (Higdon et al. 2004; Lebouteiller et al. 2010). The spectra were optimally extracted using the full aperture of the IRS short–low (SL) and long–low (LL) slits.

Since the publication of Dicken et al. (2012), there have been further updates to the data products from the *Spitzer* science center. Slight improvements to the data handling for the pipeline processing and the data fitting are mentioned in the release notes for these new versions; for example, the SMART team reports that the overall flux may be lower than previous calibrations by a few percent because of slightly different stellar templates and a different photometric calibration. We investigated the differences between the latest data products and those presented in Dicken et al. (2012) but found no significant differences. For example, the ratio of MIPS photometric flux to IRS flux at 24 μm (measured over the response range of the MIPS filter) remained similar to the ratio ($\mathrm{MIPS}_{24\,\mu\mathrm{m}}/\mathrm{IRS}_{24\,\mu\mathrm{m}} \sim 0.96$) published in Dicken et al. (2012).

3. OVERVIEW OF SPECTRA

The diversity in the mid-IR spectra of the 56 radio sources observed/detected in the 2Jy and 3CRR samples is striking (see Dicken et al. 2012, and the full version of Figure 13 in the online journal). However, many of the objects show features in common that are characteristic of AGN spectra at mid-IR wavelengths (see examples in Figure 1).

Strong fine-structure emission lines are detected in many of the spectra, with the most prominent being [Ar II] λ6.96 μm, [Ne VI] λ7.65 μm, [Ar III] λ8.99 μm, [S IV] λ10.51 μm, [Ne II] λ12.81 μm, [Ne V] λ14.32 μm, [Ne III] λ15.56 μm, [S III] λ18.71 μm, [Ne V] λ24.31 μm, and [O IV] λ25.89 μm. Two objects (PKS2356-61, 3C33) have all of these emission lines detected in their spectra, whereas the majority of spectra have varying subsets of these lines detected. In some cases this may be due to the low signal-to-noise ratio (S/N) of the spectra, but alternatively, it may reflect the differing ionization states of the emission line regions. It is noteworthy that all but one (PKS0035-02) of the 32 objects with strong optical emission lines (i.e., NLRG and BLRG/Q) have [O IV] λ25.89 μm ($E_{\mathrm{ion}} = 54.9$ eV) emission detected when available in the rest frame spectral wavelength range. The detection of this line indicates a relatively high ionization state, as expected given the presence of powerful AGNs in many of the sources. In contrast, [O IV] is detected in only 4 out of the 12 observed/detected optical WLRG, perhaps reflecting the lower AGN bolometric luminosities of these objects (Dicken et al. 2009).

Note that the [O IV] λ25.89 μm line may be blended with the lower-ionization potential [Fe II] λ25.99 μm line ($E_{\mathrm{ion}} = 7.9$ eV) in low-resolution IRS spectra. However, high spectral resolution IRS studies of powerful radio galaxies show that the ratio of [O IV]/[Fe II] is high for objects with strong [O IV] detections (Guillard et al. 2012). It is not clear that the ratio is as high for weak [O IV] detections because the features are

Table 1
2Jy Sample: Mid-IR Line Fluxes

PKS Name	z	[Ar III]	[Ne VI]	[S IV]	[Ne II]	[Ne V]	[Ne III]	[S III]	[Ne V]	[O IV]
λ (μm)		6.985	7.652	10.511	12.814	14.322	15.555	18.713	24.318	25.890
$E_{\rm ion}$ (eV)		15.8	99.1	34.8	21.6	97.1	41.0	23.3	97.1	54.9
0023−26	0.322	5.7 ± 0.2	···	···	15.9 ± 0.5	···	8.9 ± 2.7	···	···	4.5 ± 1.2
0034−01	0.073	···	···	···	3.6 ± 0.5	···	3.1 ± 1.6	···	···	<2.7
0035−02	0.220		···	···	7.5 ± 0.2	···	8.4 ± 0.7	···	···	<4.9
0038+09	0.188	6.8 ± 0.1	4.5 ± 0.5	···	12.1 ± 0.6	3.6 ± 0.6	12.5 ± 4.6	···	···	11.4 ± 1.2
0039−44	0.346	3.6 ± 0.1	17.5 ± 0.7	···	16.8 ± 2.2	26.4 ± 2.1	46.6 ± 3.1	17.1 ± 0.6	23.8 ± 2.2	91.0 ± 3.0
0043−42	0.116	···	···	···	<17.3	···	4.7 ± 0.8	···	···	<2.2
0105−16	0.400	···	···	···	<7.9	···	<5.1	···	···	or
0117−15	0.565	···	···	···	4.2 ± 0.3	···	5.4 ± 0.5	···	or	or
0213−13	0.147	···	11.8 ± 0.4	9.4 ± 0.3	9.5 ± 0.9	7.1 ± 0.5	13.3 ± 2.1	···	9.8 ± 0.5	29.6 ± 5.0
0235−19	0.620	···	···	···	8.1 ± 2.0	···	10.3 ± 0.3	···	or	or
0252−71	0.566	···	···	···	5.1 ± 0.2	···	<4.3 ± 0.6	···	or	or
0347+05	0.339	1.8 ± 0.1	···	···	10.6 ± 1.8	···	4.1 ± 1.3	···	···	<3.4
0349−27	0.066	···	···	···	9.6 ± 0.3	···	15.6 ± 0.5	···	···	15.8 ± 6.5
0404+03	0.089	···	···	···	13.6 ± 0.4	13.9 ± 0.5	18.4 ± 0.6	···	···	18.8 ± 0.6
0409−75	0.693	···	···	···	7.6 ± 1.4	···	3.8 ± 0.6	···	or	or
0442−28	0.147	···	···	···	4.3 ± 0.1	···	6.5 ± 2.3	···	···	7.4 ± 0.2
0620−52	0.051	···	···	···	2.0 ± 0.1	···	2.1 ± 0.3	···	···	2.2 ± 0.5
0625−35	0.055	···	···	···	3.4 ± 0.1	···	<5.7	···	···	<2.1
0625−53	0.054	···	···	···	<2.7	···	<3.8	···	···	<2.6
0806−10	0.110	···	98.8 ± 3.3	112.1 ± 3.7	38.1 ± 1.3	90.2 ± 5.2	145.4 ± 21.6	···	117.7 ± 3.9	365.2 ± 29.4
0859−25	0.305	···	···	6.0 ± 0.3	3.5 ± 0.6	···	11.5 ± 0.5	···	···	14.1 ± 3.2
0915−11	0.054	14.0 ± 0.5	···	···	33.3 ± 1.1	···	14.3 ± 0.8	5.2 ± 0.6	···	5.1 ± 2.4
0945+07	0.086	···	···	···	10.3 ± 1.0	···	5.4 ± 0.2	···	···	22.4 ± 0.7
1136−13	0.554	···	7.7 ± 0.3	22.7 ± 2.9	<11.7	···	11.0 ± 4.9	···	or	or
1151−34	0.258	4.2 ± 0.1	5.2 ± 0.5	5.2 ± 0.2	6.3 ± 1.2	···	11.0 ± 1.2	6.6 ± 0.7	···	12.4 ± 3.4
1306−09	0.464	···	···	···	<8.8	···	<13.2	···	or	or
1355−41	0.313	···	13.8 ± 1.6	···	<8.4	15.8 ± 0.8	<19.0	···	19.4 ± 5.3	51.5 ± 1.7
1547−79	0.483	···	13.0 ± 1.2	23.9 ± 4.6	<11.7	···	14.0 ± 1.6	···	or	or
1559+02	0.104	···	120.3 ± 4.0	103.4 ± 3.4	41.5 ± 1.4	111.5 ± 3.7	141.3 ± 4.7	···	146.8 ± 6.6	378.7 ± 17.7
1602+01	0.462	···	···	···	6.3 ± 0.6	···	<5.3	···	or	or
1648+05*	0.154	···	···	···	···	···	···	···	···	···
1733−56	0.098	···	···	6.4 ± 0.2	17.9 ± 0.6	···	17.3 ± 0.6	10.8 ± 0.8	···	16.7 ± 0.6
1814−63	0.063	···	10.8 ± 0.4	···	77.4 ± 2.6	···	62.8 ± 2.1	···	···	32.2 ± 2.5
1839−48	0.112	···	···	···	<1.5	···	<30.2	···	···	<1.7
1932−46	0.231	···	···	···	5.7 ± 1.5	···	8.6 ± 1.2	···	···	10.9 ± 0.7
1934−63	0.183	4.2 ± 0.5	3.1 ± 0.1	···	18.5 ± 2.2	···	14.1 ± 0.5	7.6 ± 0.3	···	8.4 ± 2.7
1938−15	0.452	···	···	···	6.7 ± 4.6	···	5.2 ± 1.7	···	···	or
1949+02	0.059	···	···	50.7 ± 1.7	30.7 ± 1.0	29.5 ± 1.0	58.7 ± 1.9	···	···	156.7 ± 5.2
1954−55	0.060	···	···	···	2.6 ± 0.3	···	2.5 ± 0.1	···	···	<1.6
2135−14*	0.200	···	···	···	···	···	···	···	···	···
2135−20	0.635	6.6 ± 0.5	···	$(12.1) \pm 2.8$	42.8 ± 0.4	···	23.7 ± 8.4	8.6 ± 1.6	or	or
2211−17*	0.153	···	···	···	···	···	···	···	···	···
2221−02	0.057	···	2.2 ± 0.1	289.6 ± 9.6	38.4 ± 2.8	···	99.0 ± 5.8	···	···	105.0 ± 4.7
2250−41	0.310	···	···	9.6 ± 0.3	8.4 ± 0.4	7.1 ± 1.3	13.2 ± 1.7	3.8 ± 0.1	7.5 ± 1.0	30.7 ± 1.0
2314+03	0.220	12.1 ± 0.4	···	···	60.8 ± 3.5	···	20.0 ± 0.7	···	···	26.8 ± 7.4
2356−61	0.096	7.0 ± 0.2	16.2 ± 0.5	2.8 ± 0.5	18.9 ± 0.6	11.3 ± 0.8	19.8 ± 3.8	13.2 ± 0.4	22.8 ± 0.8	55.0 ± 1.8

Notes. Table presenting prominent mid-IR line fluxes for the 2Jy sample. Units of 10^{-18} W m^{-2}. *PKS1648 was not detected by *Spitzer* IRS in our program—PKS2135-14 and PKS2211-17 were not observed as their mid-IR fluxes were deemed too low for detection.

harder to deblend when weak. Therefore, we consider it unlikely, but cannot entirely rule out, significant contamination of [O IV] fluxes by [Fe II].

Many spectra are dominated by lower-ionization potential lines such as [Ne II] $\lambda 12.81\,\mu$m ($E_{\rm ion} = 21.6$ eV), which we have detected in 43 out 56 sources (77%) in the sample, and [Ne III] $\lambda 15.56\,\mu$m ($E_{\rm ion} = 41.0$ eV), detected in 49 out of 56 sources (88%). In addition, the high-ionization potential line [Ne VI] $\lambda 7.65\,\mu$m ($E_{\rm ion} = 99.1$ eV) is detected in 34% (19/56) of the spectra, although generally at lower equivalent widths. We further note that H_2 lines (S(1) through S(7)), although not common in the samples overall, are detected in 10 out of 56 objects (18%); this is discussed further in Section 5.1. Previously, Ogle et al. (2010) detected strong H_2 emission lines in 31% of 3C and 3CRR radio galaxies at $z < 0.22$. These radio molecular hydrogen emission galaxies (radio MOHEGs) are thought to be powered by jet-shocked molecular gas.

The overall shape of the mid-IR continuum can be significantly affected by prominent 10 μm silicate emission or absorption features, as discussed in Section 1. These features are now well documented (e.g., Shi et al. 2006) and are sometimes associated with an additional less prominent feature at

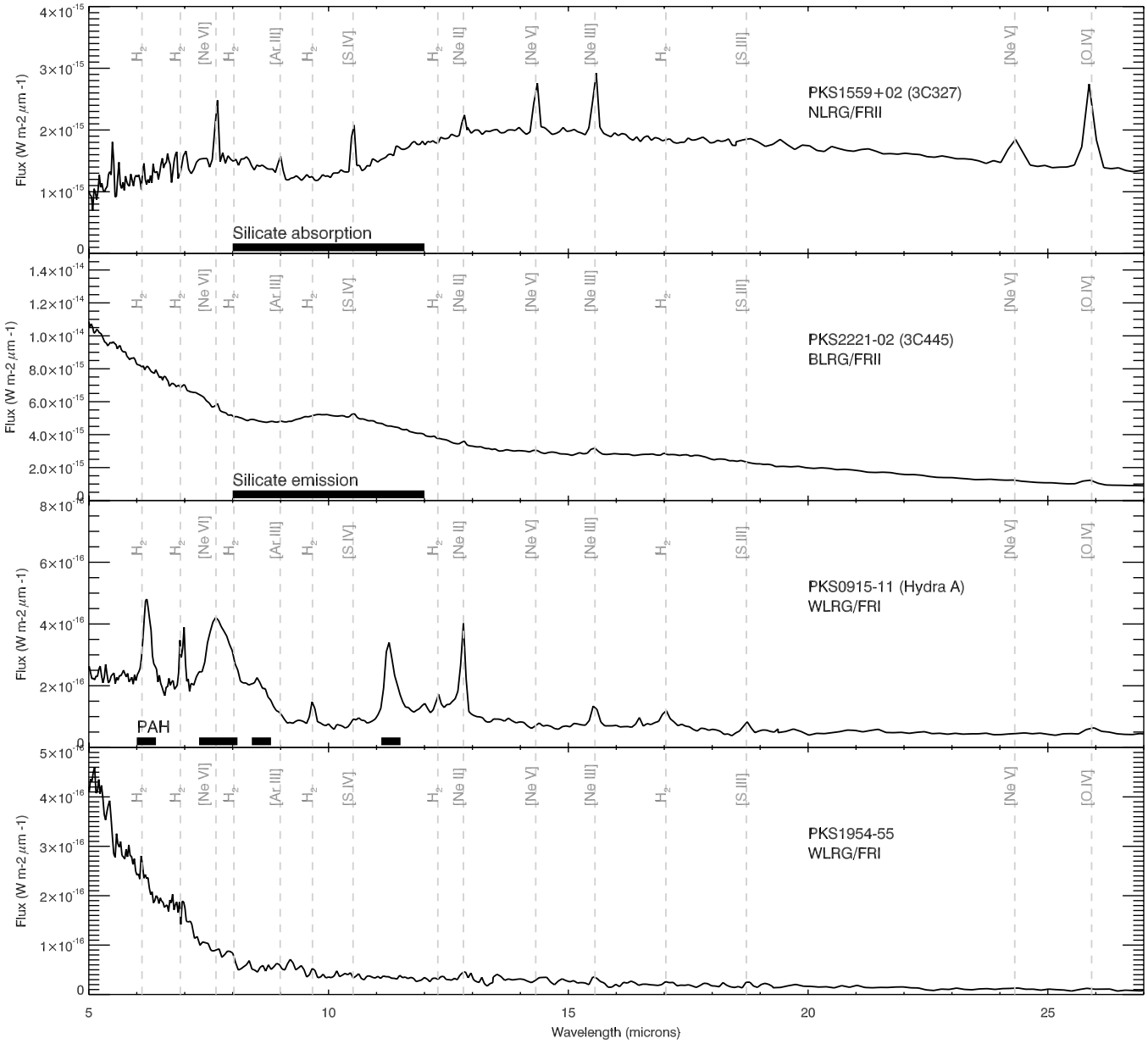

Figure 1. Examples of IRS spectra from the 2Jy sample, presenting rest frame spectra from 5 to 27 μm. From the top: PKS1559+02 shows strong mid-IR emission lines including the higher-ionization emission line ($E_{\rm ion} = 54.9$ eV) [O IV] λ25.89 μm as well as a silicate absorption at 10 μm; PKS2221-02 shows silicate emission at 10 μm; PKS0915-11 shows strong lower-ionization lines, e.g., [Ne II] λ12.81 μm ($E_{\rm ion} = 21.6$ eV) and H_2 ($S(1)$ through $S(6)$) as well as strong PAH features at 6.2, 7.7, 8.6, and 11.3 μm; PKS1954-55 shows a steep upturn in the spectrum at the blue end originating from the stellar continuum in the host galaxy.

18 μm. However, the 18 μm feature is not detected in absorption in any of the IRS spectra for the objects in our samples (see Section 6.1).

Broad, starburst-tracing, polycyclic aromatic hydrocarbon (PAH) features at 7.7 and 11.3 μm are also detected at high equivalent width in 9 out of the 56 objects with good IRS spectra. In addition, lower equivalent width 11.3 μm PAH features are detected in eight more objects. Other PAH bands that can make a significant contribution to the spectral continuum shape in the mid-IR are the 8.6 μm band and a blend of PAH emission at 17 μm (17.38 and 17.87 μm), although the latter can be strongly contaminated by H_2(S1) emission.

Finally, the contribution of starlight from the host galaxies can also affect the shape of the IRS spectra at short wavelengths ($\lambda < 8\,\mu$m). This effect is seen as a sharp upturn in flux at the blue end of the spectra and is particularly apparent for objects with low-power AGNs, for example, the WLRG PKS1839-48 and PKS1954-55.

3.1. Fitting the Spectra

In order to fit the spectra we used PAHFIT v1.2,[21] which is an IDL program developed by J. D. T. Smith and B. T. Draine to study PAH features in the mid-IR spectra of the inner regions of local star-forming galaxies (Smith et al. 2007). The fitted spectra for all objects are presented in the online journal. We experimented with, and adapted, the PAHFIT code to check and improve its performance for the samples of powerful radio-loud AGNs presented in this study. First, we experimented with adding dust components into the model with blackbody

[21] PAHFIT is made available under the terms of the GNU General Public License.

temperatures 400, 600, 1000, and 2000 K in order to account for the potential hotter dust continuum features due to the powerful AGN, but the PAHFIT model fitted the data just as well without these extra hot components. Therefore, we returned the code to the default model continuum dust temperatures (300, 135, 90, 65, 50, 40, 35 K). However, it is notable that in fitting the blue end of the spectrum, where the hot dust components would be, the PAHFIT program adds a stellar continuum component, which could be compensating for the lack of hot dust components in the model instead of tracing the stellar continuum. Because we are not directly interested in the hot dust or stellar contribution in this paper, the fit to the continuum seen in the PAHFIT results is adequate for our purposes.

Second, when fitting the 10 and 18 μm silicate absorption features, we found that the default PAHFIT extinction model, based on the dust opacity law of Kemper et al. (2004), did not fit the features well. After some experimentation it was found that the depth of the silicate absorption feature was better fitted in models assuming high ratios of 10–18 μm opacity. This implies that the 18 μm absorption feature is weak for our samples of powerful radio-loud AGNs, as we discuss further in Section 6.1.

Third, by default PAHFIT includes PAH features in the model fitted to the spectra. However, in Dicken et al. (2012) we found little direct evidence for PAH features and/or the starburst activity often associated with such emission in the vast majority of objects. Therefore, in this investigation, when fitting the spectra with PAHFIT to measure the fluxes of the fine-structure lines, we only included PAH features in the model for objects with confirmed detections of the 11.2 μm feature (see Table 5 in Dicken et al. 2012). It is notable that the PAHFIT model without the PAH components still fits the observed spectra well in the objects without evidence for PAH.

Finally, the original PAHFIT model does not include silicate emission because objects with such emission were not included in the sample that PAHFIT was originally designed to fit (Smith et al. 2007). However, the 10 μm silicate emission feature is clearly detected at varying strengths in 25% of the observed/detected objects in the 2Jy and 3CRR samples. Therefore, we made a further adaptation of the PAHFIT program to fit silicate emission as well as absorption, following the method employed in Gallimore et al. (2010). This entailed adding a model for warm dust clouds that are optically thin at infrared wavelengths. This assumes that the clouds have a simple slab geometry and opacity at 10 μm, $\tau_{10} < 1$. These warm clouds are further assumed to be partially covered by cold, absorbing dust clouds, and the source function is a scaled Planck spectrum at the fitted temperature for simplicity.

The PAHFIT measurements of the most prominent mid-IR emission lines are presented in Tables 1 and 2, while the H_2 detections and silicate emission/absorption strengths are presented in Tables 3 and 5.

PAHFIT returns formal statistical uncertainties on the emission line fits. However, given the wide range of factors affecting the quality of these measurements, we found these formal uncertainties to be unrealistically small in many cases. In addition, PAHFIT may return an emission line measurement when, in fact, it has just fitted a particular line to the fluctuations in the noise. Therefore, we adopted a more robust approach to the emission line detection and uncertainty calculations.

In determining whether a particular feature was detected, we first visually inspected all the spectra for candidate detections. Following this, we refitted the data for each of the two nod positions of the observations and measured the difference in emission line flux between these two spectra. If the difference in the line flux between the two nod position measurements was less than 20%, we considered this a confident detection. Objects that had differences between 20% and 50% were reconfirmed or rejected by visual inspection. Note that the S/N improves in the combined nodded spectra, which adds weight to these weaker detections. The uncertainties presented are the differences between the mean flux in the averaged nod position spectra and the fluxes in the individually nodded spectra, the calibration uncertainty of 3.3%,[22] or the PAHFIT uncertainty, whichever was greater. Note the uncertainties for the spectra that were obtained in mapping mode may be underestimated because they do not have nodded data for comparison. These lines were identified visually, and the quoted error is either the calibration uncertainty or the PAHFIT uncertainty, whichever is greater.

Also, in Tables 1 and 2 we present upper limits for the main emission lines ([Ne II] λ12.81 μm, [Ne III] λ15.56 μm, [O IV] λ25.89 μm) used in this investigation for objects in which these lines were not clearly detected. These upper limits were derived by using, as a template, the IRS spectrum of PKS2356-61, which has clearly detected narrow emission lines and little evidence for contaminating PAH emission. After the silicate absorption fitted in the PAHFIT model has been subtracted, the spectrum of PKS2356-61 is added to the spectrum of each object without detected emission lines. A multiplicative scaling factor for the template spectrum was then varied until the appropriate emission line feature was just detected in a visual inspection of the combined spectrum. Multiplying the measured emission line flux for PKS2356-61 by the scaling factor then gives a robust upper limit on emission line flux. For high-redshift objects the [Ne II] λ12.81 μm line is redshifted from the SL module to the LL module. Therefore, for consistency, we used the spectrum of the higher-redshift object PKS2250-41 to measure the upper limits for sources where this line was observed in the LL module rather than SL.

4. AGN POWER INDICATORS

The mid-IR spectral line [O IV] λ25.89 μm is a good candidate for an AGN power indicator because it has a relatively high ionization potential ($E_{\rm ion} = 54.9$ eV), which favors an AGN rather than a starburst origin. This feature lies toward the longer-wavelength end of the IRS spectral range and so is less likely to suffer from the effects of dust extinction. We note that, in the case of the 2Jy and 3CRR samples, the mid-IR [O IV] λ25.89 μm line is detected in all but one of the objects with strong optical emission lines for which [O IV] lies in the wavelength range of the IRS instrument ($z < 0.350$).

To investigate whether the [O IV] line emission indeed has an AGN origin for the 2Jy and 3CRR objects, we compare it to other AGN power indicators from our extensive archive of complementary observations at optical, infrared, radio, and X-ray wavelengths.[23]

For the initial analysis, we do not include the objects classified as WLRG at optical wavelengths. Mounting evidence

[22] Note that the flux calibration is anchored at 24 μm, with an uncertainty of the order of 3% (G. C. Sloan 2012, private communication). Therefore, toward shorter wavelengths the uncertainty will increase by several percent because the spectrum moves through several orders and changes module once.

[23] The *Spitzer* mid- to far-infrared, [O III], and 5 GHz luminosities used in the following investigation are presented in Dicken et al. (2008) and Dicken et al. (2010) for the 2Jy and 3CRR samples, respectively. X-ray luminosities were taken from the study of Mingo et al. (2013).

Table 2
3CRR Sample: Mid-IR Line Fluxes

Name	z	[Ar III]	[Ne VI]	[S IV]	[Ne II]	[Ne V]	[Ne III]	[S III]	[Ne V]	[O IV]
λ (μm)		6.985	7.652	10.511	12.814	14.322	15.555	18.713	24.318	25.890
$E_{\rm ion}$ (eV)		15.8	99.1	34.8	21.6	97.1	41.0	23.3	97.1	54.9
3C33	0.060	13.4 ± 0.4	27.9 ± 0.9	16.3 ± 0.5	33.9 ± 1.1	14.4 ± 0.5	48.7 ± 1.6	27.3 ± 0.9	13.4 ± 1.4	72.9 ± 2.4
3C35*	0.067	...	...	...	...	...	...	...	...	...
3C98	0.030	...	...	...	10.1 ± 1.0	...	23.3 ± 0.8	...	...	44.2 ± 1.5
3C192	0.060	...	...	...	6.2 ± 0.4	...	4.8 ± 1.7	6.0 ± 2.4	...	22.8 ± 0.8
3C236	0.101	...	...	...	19.9 ± 2.0	...	<21.9	...	...	<11.0
3C277.3*	0.085	...	...	...	...	...	...	...	...	...
3C285	0.079	...	...	15.0 ± 0.5	18.5 ± 0.6	...	34.2 ± 1.1	...	15.3 ± 0.5	56.8 ± 1.9
3C293	0.045	29.9 ± 1.0	...	...	73.2 ± 2.4	...	30.5 ± 1.0	9.0 ± 1.6	...	5.6 ± 2.0
3C305	0.042	...	...	51.2 ± 1.7	42.9 ± 1.4	27.5 ± 0.9	147.9 ± 4.9	36.7 ± 1.2	35.1 ± 1.2	189.6 ± 6.3
3C321	0.096	...	114.0 ± 3.8	137.0	26.2 ± 0.9	140.3 ± 9.9	210.5 ± 6.9	18.0 ± 6.9	207.2 ± 9.9	736.6 ± 32.9
3C326	0.090	...	...	...	<2.8	...	<59.2	...	...	<3.3
3C382	0.058	0.6 ± 0.1	71.5 ± 2.4	88.8 ± 2.9	28.4 ± 0.9	9.6 ± 0.6	46.3 ± 1.5	...	11.2 ± 1.7	30.5 ± 1.0
3C388	0.092	...	...	...	<2.8	...	<4.9	...	...	2.4 ± 0.6
3C390.3	0.056	13.1 ± 0.4	8.0 ± 1.5	17.2 ± 1.2	42.0 ± 1.4	...	30.6 ± 1.0	...	...	25.5 ± 0.8
3C452	0.081	7.8 ± 1.7	4.0 ± 0.8	2.7 ± 0.8	19.4 ± 1.1	...	21.0 ± 3.4	6.0 ± 1.2	...	11.8 ± 0.4
4C73.08*	0.058	...	...	...	...	...	...	...	...	...
da240*	0.036	...	...	...	...	...	...	...	...	...

Notes. Table presenting prominent mid-IR line fluxes for the 3CRR sample. Units of 10^{-18} W m^{-2}. *3C35 and 3C277.3 were not detected in the observations taken in mapping mode, and 4C73.08 and da240 do not have IRS data available in the *Spitzer* archive.

Table 3
Combined Sample Spearman Rank Statistics

Rank Correlation	n	r_s	Significance	r_s (ASURV)	Significance
Basic rank correlation statistics					
$L_{[\rm O\,IV]}$ vs. $L_{[\rm O\,III]}$	32	0.79	>99.9%	0.78	>99.9%
$L_{[\rm O\,IV]}$ vs. L_{24}	32	0.81	>99.9%	0.79	>99.9%
$L_{[\rm O\,IV]}$ vs. $L_{5\,\rm GHz}$	32	0.55	>99.9%	0.53	>99.9%
$L_{[\rm O\,IV]}$ vs. $L_{\rm X\text{-}ray}$	32	−0.01	≪50%	−0.003	≪50%
$L_{[\rm Ne\,III]}$ vs. $L_{[\rm O\,III]}$	44	...	...	0.75	>99.9%
$L_{[\rm Ne\,III]}$ vs. L_{24}	44	...	...	0.76	>99.9%
$L_{[\rm O\,III]}$ vs. L_{24}	44	...	...	0.86	>99.9%
Partial rank correlation with z					
$L_{[\rm O\,IV]}$ vs. $L_{[\rm O\,III]}$	32	0.63	>99.9%	0.62	>99.9%
$L_{[\rm O\,IV]}$ vs. L_{24}	32	0.67	>99.9%	0.65	>99.9%
$L_{[\rm O\,IV]}$ vs. $L_{5\,\rm GHz}$	32	−0.24	≪50%	−0.22	≪80%
$L_{[\rm O\,IV]}$ vs. $L_{\rm X\text{-}ray}$	32	−0.27	≪50%	0.17	≪50%

Notes. Results of various Spearman rank correlation tests for the combined 3CRR and 2Jy sample for the correlations presented in Figure 2. These tests do not include weak-line radio galaxies, but do include one object (PKS0035-02) with an [O IV] upper limit value and the five objects with X-ray upper limits which are included in the test as if they were detections. Values of $-1 < r_s < 1$ are given for each correlation, where a value close to 1 or −1 is highly significant. Columns 2 and 3 present the results of the Spearman rank statistics; note the single upper limit in $L_{[\rm O\,IV]}$ values was treated as a detections for the purposes of these test. Columns 4 and 5 present statistics for all the objects in the combined sample, handling the upper limits using survival analysis statistics.

Table 4
H_2 Fluxes

Name	z	$H_2(S3)$	$H_2(S2)$	$H_2(S1)$
0023−26	0.322	4.0 ± 0.1	5.2 ± 4.1	10.4 ± 1.8
0915−11	0.054	16.3 ± 1.2	6.3 ± 0.2	9.1 ± 1.9
1151−34	0.258	5.3 ± 0.2	2.5 ± 0.9	4.1 ± 0.1
1733−56	0.098	3.7 ± 0.1	0.5 ± 0.2	10.3 ± 0.4
1814−63	0.063	7.6 ± 0.3	8.7 ± 0.3	18.2 ± 6.1
3C33	0.060	<ul	<ul	9.2 ± 1.1
3C285*	0.079	8.4 ± 0.3	12.5 ± 0.4	26.5 ± 0.0
3C293	0.045	97.6 ± 3.2	22.7 ± 0.7	74.8 ± 3.6
3C305	0.042	27.9 ± 0.9	11.9 ± 0.4	33.1 ± 1.1
3C326	0.090	<ul	<ul	7.4 ± 2.8

Notes. Units of 10^{-18} W m^{-2}. *3C285 observed in mapping mode, therefore uncertainties may be underestimated, see Section 3.1.

suggests that these objects are fundamentally different from optical strong-line radio galaxies (e.g., Hardcastle et al. 2007; Buttiglione et al. 2010). In particular, they have been associated with different accretion modes for the central supermassive black holes (e.g., Hardcastle et al. 2007). Moreover, the detection rate of [O IV] for the WLRG in the two samples is low (only 2/12 observed/detected objects). This is to be expected if WLRG have intrinsically weak AGNs (e.g., Ogle et al. 2006; Dicken et al. 2009), so that the higher-ionization lines, such as [O IV], are less likely to be detected (see Section 7.3 for further discussion).

Figure 2 plots $L_{[\rm O\,IV]}$ against four other candidate AGN power indicators: [O III] λ5007 optical emission line luminosity ($L_{[\rm O\,III]}$[24]), mid-infrared luminosity at 24 μm ($L_{24\,\mu\rm m}$), total radio luminosity at 5 GHz ($L_{5\,\rm GHz}$), and accretion-related X-ray luminosity ($L_{\rm X\text{-}ray}$)[25] for the combined sample. Figure 2 only includes objects with redshifts $z < 0.350$ for which the [O IV] line is available in the wavelength range of *Spitzer* IRS. This excludes 11 objects from the higher-redshift range of the 2Jy sample.

$L_{[\rm O\,III]}$, $L_{24\,\mu\rm m}$, $L_{5\,\rm GHz}$, and $L_{\rm X\text{-}ray}$ are widely accepted to have an AGN origin in radio galaxies: optical [O III] emission arises from narrow-line region clouds that are directly heated

[24] $L_{[\rm O\,III]}$ values are corrected for Galactic extinction.

[25] We use the X-ray accretion-related component here as a proxy for AGN power, rather than the X-ray unabsorbed component, which is likely to be affected by beaming because it is emitted by the jet. The accretion-related X-ray luminosity has been integrated over energies 2–10 keV assuming an intrinsic power-law continuum shape (see Mingo et al. 2013 for further details).

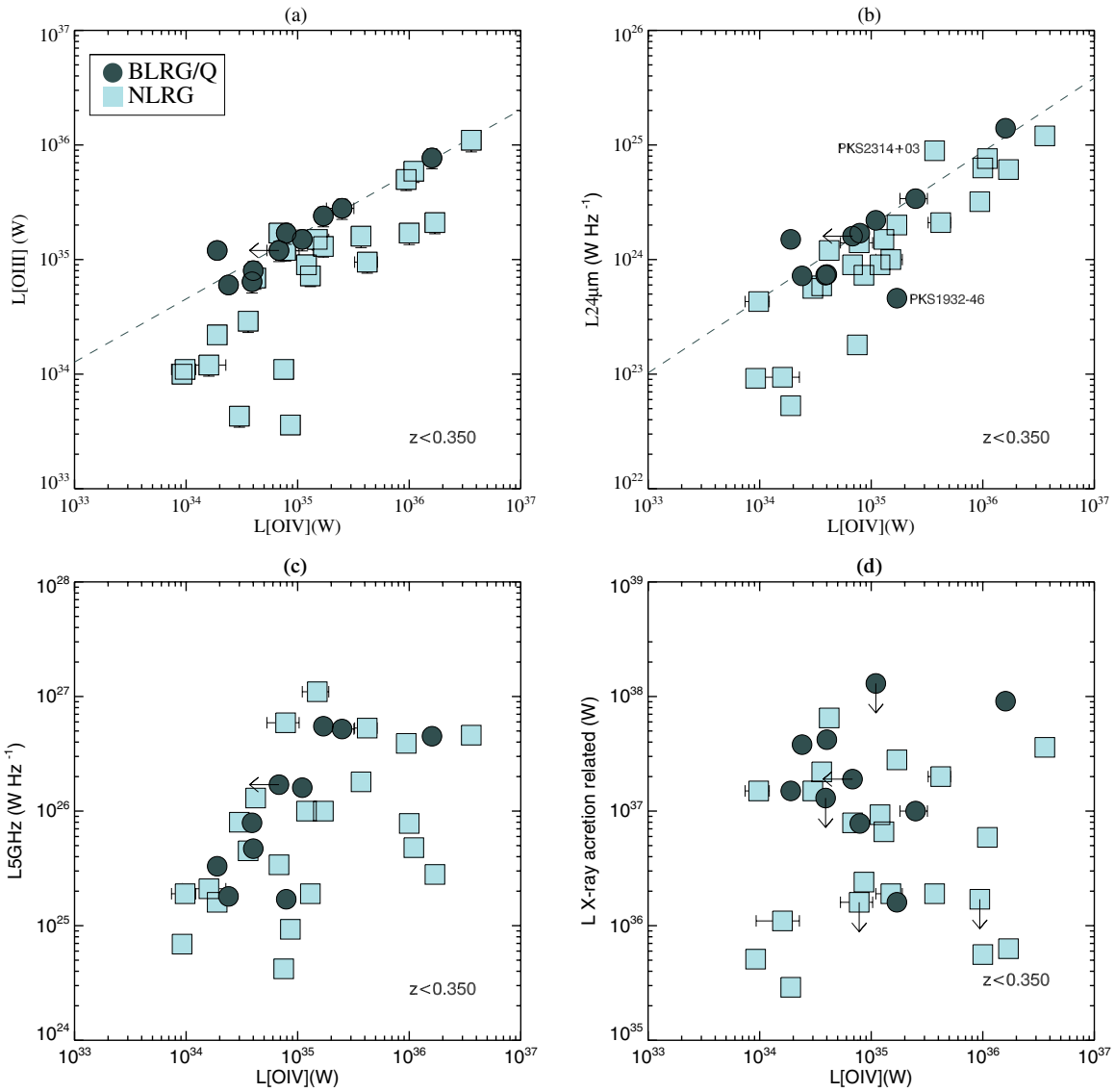

Figure 2. Plot showing $L_{[\mathrm{O\,IV}]\,\lambda 25.89\,\mu\mathrm{m}}$ vs. $L_{[\mathrm{O\,III}]\,\lambda 5007}$, $L_{24\,\mu\mathrm{m}}$, $L_{5\,\mathrm{GHz}}$, and $L_{\mathrm{X\text{-}ray}}$ with objects identified by optical classes. The samples are limited to objects with $z < 0.350$ due to the requirement that the [O IV] line fall in the redshift range of *Spitzer*/IRS. In order to maintain a comparable range in the x and y axes, (d) excludes the object 3C305, which has a low upper limit value $L_{\mathrm{X\text{-}ray}} < 8.9 \times 10^{33}$. Optical classifications are BLRG/Q, broad-line radio galaxy/quasar, and NLRG, narrow-line radio galaxy. Uncertainties are plotted for all data points but are typically smaller than the object marker. The regression lines fitted in (a) and (b) are fitted to the BLRG/Q objects. See Section 5 for a discussion of PKS1932-46 and Section 6.2 for a discussion of PKS2314+03.

(A color version of this figure is available in the online journal.)

by the AGN. In the absence of strong star formation, the 24 μm continuum emission originates from warm/hot dust situated relatively close to, and heated directly by, the AGN. Low-frequency radio lobe emission is known to be isotropic and is powered by the relativistic jets originating from the AGN; here we use the complete data set of total 5 Ghz radio fluxes that are available for all the sample objects. This is a relatively high radio frequency band, but because of the steep-spectrum selection and the careful analysis detailed in Dicken et al. (2008) we are certain that the potential effect of beaming at these higher frequencies is minimal for the strong-line objects in the 2Jy sample. Last, the accretion-related X-ray emission originates from, or close to, the accretion disk associated with the AGN.

From Figure 2 it is clear that $L_{[\mathrm{O\,III}]}$ and $L_{24\,\mu\mathrm{m}}$ are strongly correlated with $L_{[\mathrm{O\,IV}]}$, whereas the correlations are much weaker for $L_{5\,\mathrm{GHz}}$ and $L_{\mathrm{X\text{-}ray}}$. Spearman rank statistics for the four correlations shown in Figure 2 are presented in Table 3. The top section of Table 3 presents the basic rank statistics, which shows that all the AGN power proxies correlate significantly with $L_{[\mathrm{O\,IV}]}$ apart from X-ray luminosities; the null hypothesis that the variables are unrelated is rejected at the >99.5% confidence level. The correlations between $L_{[\mathrm{O\,IV}]}$ and $L_{[\mathrm{O\,III}]}$, $L_{24\,\mu\mathrm{m}}$, and $L_{5\,\mathrm{GHz}}$, which are common indicators of AGN power, give weight to the hypothesis that $L_{[\mathrm{O\,IV}]}$ is also a reliable AGN power indicator.

Although the majority of the basic correlation statistics support the use of $L_{[\mathrm{O\,IV}]}$ as an AGN power proxy, it is important to test whether the correlations are intrinsic and not due to the increase in luminosity with redshift in the flux-limited samples. Therefore, in the second section of Table 3, we present Spearman partial rank correlation tests. These tests are aimed at determining whether the correlations only arise because the variables are independently correlated with a third variable, in this case redshift. The results of the partial correlation tests show that we can still reject the null hypothesis that the variables

are unrelated at the >99.5% level of significance for the correlations with $L_{[O\,III]}$ and $L_{24\,\mu m}$ but not for the $L_{[O\,IV]}$ versus $L_{5\,GHz}$ correlation. In the case of $L_{X\text{-}ray}$ we find no statistically significant correlation with $L_{[O\,IV]}$ in our investigation.

The null result for the partial rank $L_{[O\,IV]}$ versus $L_{5\,GHz}$ correlation test reflects the scatter seen in Figure 2(c) and agrees with our previous work (Dicken et al. 2009), where we found that the correlation between $L_{[O\,III]}$ and $L_{24\,\mu m}$ has greater significance than the correlation between $L_{5\,GHz}$ and $L_{24\,\mu m}$. As mentioned in Section 1, the lack of correlation with $L_{5\,GHz}$ may be due to the bulk of the radio emission originating hundreds of kiloparsecs from the nucleus, introducing a time lag between the recent power level of the AGN (as traced by $L_{[O\,IV]}$) and that of the radio emission. Alternatively, the luminosity of the radio emission could also depend on secondary factors other than intrinsic AGN power, such as the properties of the ISM in the halo of the host galaxy into which the jets and lobes expand (Barthel & Arnaud 1996). It is also noteworthy that Mingo et al. (2013) found a better correlation between radio luminosity and jet-related X-ray luminosity.

Statistically significant correlations between $L_{[O\,III]}$ and $L_{X\text{-}ray}$ were seen in the studies of Hardcastle et al. (2009) and Mingo et al. (2013). For the sample included in this paper we find no significant correlation between $L_{[O\,III]}$ and $L_{X\text{-}ray}$ ($r_s = 0.12$, confidence level of 50%). The difference between our results and those of Hardcastle et al. (2009) and Mingo et al. (2013) can be explained in terms of the large intrinsic scatter for the correlations combined with the smaller size, and more restricted redshift/luminosity range of the 2Jy sample relative to the 3CR. This large apparent scatter in correlations involving $L_{X\text{-}ray}$ may be caused by short-term variability in the X-ray source that is not seen for $L_{[O\,III]}$ and 24 μm luminosities, because these are emitted on larger scales and therefore integrate the power of the AGN over longer timescales. In the case of the *XMM* observations used for the higher-redshift objects, it is also possible that the X-ray emission of the target objects is contaminated by neighboring sources or emission from hot X-ray halos of the host galaxies/clusters. Finally, uncertainties in the correction for the gas absorption and separating the nonthermal X-ray emission from the jets might also contribute to the scatter. We note that a similarly larger scatter in the correlations involving $L_{X\text{-}ray}$ and $L_{5\,GHz}$ was also seen in the analysis of intrinsic AGN power indicators in Seyfert galaxies by LaMassa et al. (2010). Our sample is also significantly smaller and covers a more restricted range in redshift/luminosity than that of Mingo et al. (2013). However, even with the smaller sample, $L_{[O\,IV]}$, $L_{[O\,III]}$, and $L_{24\,\mu m}$ still show significant correlations in our analysis. Therefore, we conclude that the latter are better bolometric indicators of AGN power than $L_{X\text{-}ray}$.

As a comparison to our statistical method, and to take into account the effect of the one $L_{[O\,IV]}$ upper limit for PKS0035-02 included in the previous tests as a detection, as well as the five upper limits in $L_{X\text{-}ray}$, the above Spearman rank tests were also conducted using survival statistics in the ASURV package (Isobe et al. 1986; Lavalley et al. 1992), as implemented in IRAF. The results of the ASURV Spearman rank tests are presented in Columns 4 and 5 of Table 3 and are consistent with those of the basic tests, albeit with slightly lower r_s values.

A disadvantage of using the [O IV] λ25.89 μm line is that it is redshifted out of the spectral range of the IRS instrument for objects with redshifts $z \geqslant 0.35$. This affects 11 out of 46 objects in the higher-redshift half of the 2Jy sample. Therefore, we also investigate correlations involving the [Ne III] λ15.56 μm line, which has a relatively high ionization energy ($E_{ion} = 41.0$ eV) and may also have an AGN origin, following arguments similar to those presented above for [O IV]. However, [Ne III] has a lower ionization energy than [O IV] and therefore is more likely to have a significant contribution from stellar photoionization; also, its shorter wavelength may make it more susceptible to obscuration.

To test the value of [Ne III] λ15.56 μm as an alternative AGN power proxy, we have plotted $L_{[Ne\,III]}$ against $L_{[O\,III]}$ and $L_{24\,\mu m}$ in Figure 3. Strong correlations between these quantities can clearly be seen in Figures 3(a) and (b), and the correlations are confirmed with the ASURV[26] Spearman rank statistical tests presented in Table 3. These show that we can reject the null hypothesis that the variables are unrelated at a >99.5% level. However, we note that the correlations of $L_{[Ne\,III]}$ with $L_{[O\,III]}$ and $L_{24\,\mu m}$ have lower statistical significance than those of $L_{[O\,IV]}$ with $L_{[O\,III]}$ and $L_{24\,\mu m}$, despite the larger sample ($n = 44$ and 34 for the tests with [Ne III] and [O IV], respectively). We conclude that [Ne III] λ15.56 μm is a good AGN proxy for powerful radio galaxies, but less so than [O IV] λ25.89 μm, as further supported by the results presented in Section 5.

5. DEGREE OF ANISOTROPY

Previously, in Dicken et al. (2009, 2010), we investigated the isotropy of the optical [O III] emission in the 2Jy sample. Despite a large scatter in the results, we found evidence that BLRG/Q showed a tendency to fall below the $L_{[O\,III]}$ versus $L_{70\,\mu m}$ correlation, but on the $L_{[O\,III]}$ versus $L_{24\,\mu m}$ correlation defined by the NLRG. In agreement with the orientation-based unified schemes, this result can be explained if both the [O III] and 24 μm emissions, but not the 70 μm emission, in NLRG suffer a mild degree of dust extinction (e.g., by a dust torus); however, this previous work was not statistically conclusive. We now return to this investigation with the new mid-IR emission line data.

The optical classifications of the combined sample objects are indicated in Figures 2 and 3. From a detailed inspection of Figure 2(a) it is clear that the BLRG/Q are offset from the NLRG by typically 0.2–1.0 dex, tending to the upper edge of the correlation between $L_{[O\,IV]}$ and $L_{[O\,III]}$. In Figure 2(b) we find a similar offset is also apparent for the $L_{[O\,IV]}$ versus $L_{24\,\mu m}$ correlation.[27] Figures 3(a) and (b) also show a similar result for the correlations between $L_{[Ne\,III]}$, $L_{[O\,III]}$, and $L_{24\,\mu m}$. In addition, there is evidence that the difference is larger for objects with lower AGN powers: below $L_{[O\,IV]} = 10^{35}$ W there is a group of NLRG objects that lies ~1.5 to 2 dex below the correlation defined by the BLRG/Q.

The [O IV] and [Ne III] lines and the 24 μm continuum are emitted within the same mid-IR wavelength range. Therefore, naively, one might expect that any obscuration that affects the 24 μm continuum will also affect the [O IV] and [Ne III] lines to a similar degree. However, whereas much of the 24 μm continuum emission is thought to be emitted by the inner parts of the torus (<10 pc) and therefore could potentially suffer significant dust extinction in the NLRG objects, even at these relatively long wavelengths, the [O IV] and [Ne III] are likely to be emitted on the much larger scales of the narrow-line region (NLR; 10–1000 pc)

[26] We only use ASURV statistics in this analysis due to the five upper limits on the [Ne III] emission.

[27] We note that the outlier BLRG that lies under the correlation of Figures 2(b) and 3(b) is PKS1932-46. This object has been uniquely identified with an underluminous AGN that is proposed to have just switched to a low-activity phase; see Inskip et al. (2007) for details.

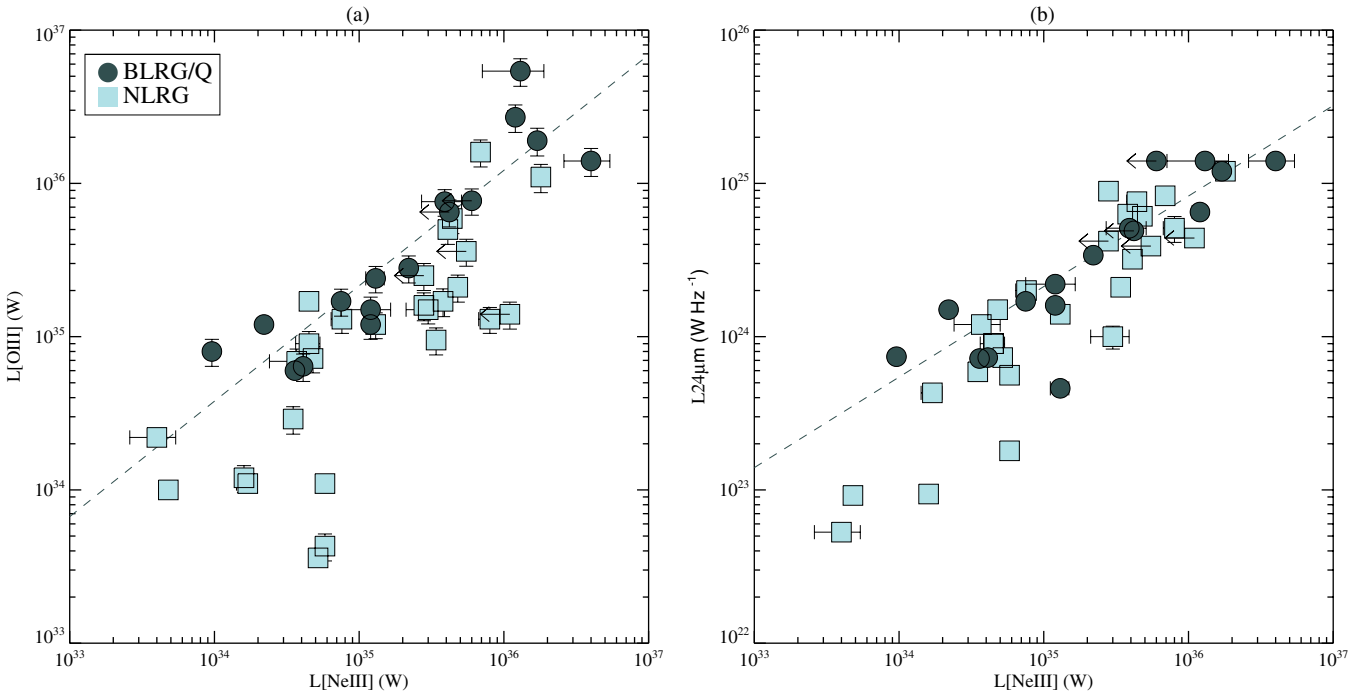

Figure 3. Plot showing $L_{[\mathrm{Ne\,III}]\,\lambda 15.56\,\mu\mathrm{m}}$ vs. $L_{[\mathrm{O\,III}]\,\lambda 5007}$ and $L_{24\,\mu\mathrm{m}}$ with objects identified by optical classes; see Figure 2 for definitions. The linear regression results for the BLRG/Q objects are shown as dashed lines.

(A color version of this figure is available in the online journal.)

for which the level of dust extinction is relatively modest in the mid-IR (but more significant, of course, for optical emission lines such as [O III] λ5007).

To visualize the evidence for anisotropy in another way, we can study the ratios of [O III]/[O IV] and 24 μm/[O IV] as well as [O III]/[Ne III] and 24 μm/[Ne III]. Assuming that the [O IV] and [Ne III] lines are emitted isotropically, dividing the fluxes of the [O III] and 24 μm emissions by those of the mid-IR lines serves to highlight any difference between the optical classes of objects due to obscuration. Figure 4 plots [O III]/[O IV] versus 24μm/[O IV], where a loose correlation with some scatter can be seen. A caveat to this investigation is that the [O III]/[O IV] ratio may be affected by ionization effects that also increase the scatter. As expected from Figures 2(a) and (b), the BLRG/Q have, on average, higher ratios of [O III]/[O IV] and 24 μm/[O IV] than the NLRG, and the scatter is greater for the NLRG than for the BLRG/Q.[28] Figure 4(a) confirms that the same NLRG that have evidence of attenuation of $L_{[\mathrm{O\,III}]}$ compared to BLRG/Q also have evidence of attenuation of $L_{24\,\mu\mathrm{m}}$, suggesting that both types of emission are significantly attenuated in these objects. We have also plotted the ratios as histograms in Figures 4(c) and (d), separating BLRG/Q and NLRG. The degree of attenuation of the [O III] and 24 μm emissions can be quantified using the median ratio values for the two optical classes: [O III]/[O IV] = 1.6 (BLRG/Q) and 0.7 (NLRG), and 24 μm/[O IV] = 1.9 (BLRG/Q) and 0.8 (NLRG); both sets of numbers imply a factor of ∼2.3 attenuation in the NLRG relative to the BLRG/Q objects.

Although the degree of attenuation appears to be to the same for [O III] and 24 μm and in broadly the same objects, it is clear that a factor of 2.3 attenuation at 5007 Å implies a much lower visual dust extinction (A_V) than a similar factor at 24 μm. For example, to attenuate the [O III] by a factor of 2.3, we would require $A_V \sim 0.8$ visual extinction compared to $A_V \sim 20$–100 (depending on the extinction law; Mathis 1990; Draine 2003) implied by the 24 μm results. Therefore, the absorbing dust columns must be different in the two cases. It is also the case that if the [O IV] is emitted by the same region as the [O III], it will suffer lower extinction ($A_V \sim 0.1$). This supports our assumption that the [O IV] is unattenuated.

To put the results from Figures 2(a) and (b) on a firmer statistical footing, we have considered the vertical displacements of the BLRG and NLRG objects from a linear regression line fitted to the BLRG/Q objects alone. The results are presented in Figure 5, where we show histograms of the distribution of displacements for the BLRG/Q and NLRG. Using a one-dimensional (1D) Kolmogorov–Smirnov (KS) test, we can reject the null hypothesis that the BLRG/Q and NLRG samples are drawn from the same population at better than a 99% significance level for the $L_{[\mathrm{O\,IV}]}$ versus $L_{[\mathrm{O\,III}]}$ and $L_{[\mathrm{O\,IV}]}$ versus $L_{24\,\mu\mathrm{m}}$ correlations.[29] Using the regression line fitted to the BLRG/Q objects in Figure 2(a) as a reference, we find that the NLRG lie a median factor of 2.7 (mean factor of 5.5 ± 0.3) below the BLRG/Q in $L_{[\mathrm{O\,III}]}$ for a given AGN power, as traced by $L_{[\mathrm{O\,IV}]}$. The ranges of attenuation factors derived using this technique are consistent with those derived above using the line ratios.

To include the 11 higher-redshift objects that have [O IV] redshifted outside of the spectral range of *Spitzer* IRS, we repeat the investigation in Figure 4(b), replacing [O IV] with [Ne III]. From the histograms in Figures 4(e) and (f), the line ratios relative to [Ne III] show a difference for [O III] but not for the 24 μm emission, where the median ratio values are

[28] The NLRG outlier above the correlation, PKS1814-63, is a rare example of a radio source in a disk galaxy (Morganti et al. 2011). It is possible that star formation in the disk could be contributing to its 24 μm emission.

[29] The tests were conducted with and without the one upper limit in [O IV] and the five upper limits in [Ne III] with no significant change in the results.

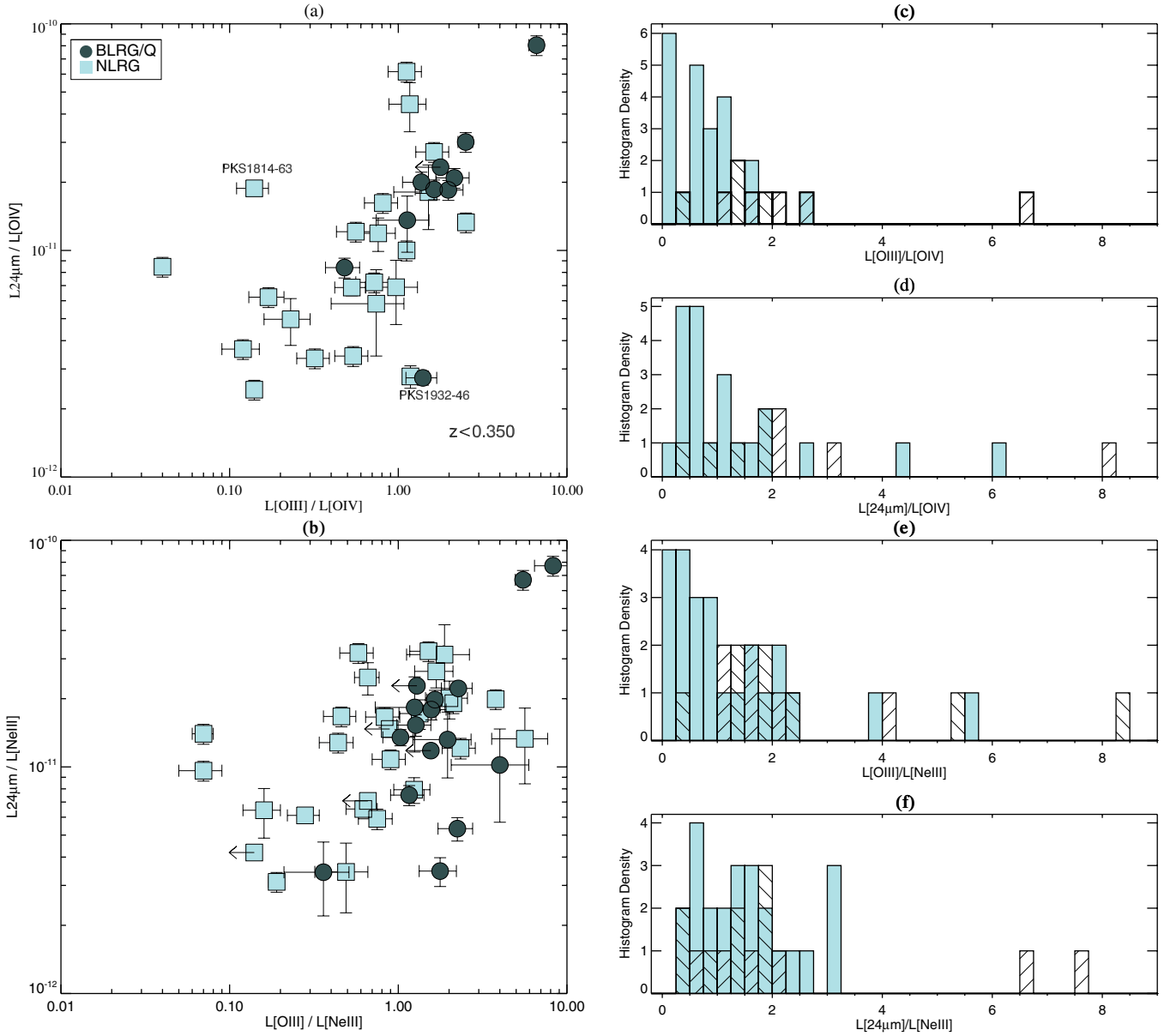

Figure 4. Comparisons of diagnostic ratios [O III] λ5007/[O IV] λ25.89 μm and 24 μm/[O IV] λ25.89 μm as well as [O III] λ5007/[Ne III] λ15.56 μm and 24 μm/[Ne III] λ15.56 μm. The upper limit in [O IV] for PKS0035-02 is plotted in (a) but not in (c) and (d). The five upper limits in [Ne III] results are plotted in (b) but not in (e) and (f). Ratio value presented in (d) and (f) are in units of 10^{11}. See Figure 2 for plot symbol definitions. Crossed bars in the histograms are BLRG/Q, and filled bars are NLRG.

(A color version of this figure is available in the online journal.)

[O III]/[Ne III] = 1.7 (BLRG/Q) and 0.8 (NLRG) and 24 μm/[Ne III] = 1.4 (BLRG/Q) and 1.4 (NLRG). For the correlations between $L_{[\mathrm{Ne\,III}]}$ and $L_{[\mathrm{O\,III}]}$ the 1D KS tests show we can reject the null hypothesis that the BLRG/Q and NLRG samples are drawn from the same population at no better than a 90% level of significance. Testing the $L_{[\mathrm{Ne\,III}]}$ versus $L_{24\,\mu\mathrm{m}}$ correlation, we find that we can reject the null hypothesis at the <90% level of significance for tests both with and without PKS1932-46. These tests confirm what is readily identifiable by eye: the offset between the BLRG/Q and NLRG in Figure 3 is not as significant as seen in Figures 2(a) and (b). Plausibly, [Ne III] emission is subject to a greater degree of extinction than the longer-wavelength [O IV] emission, and photoionization by stars may make a significant contribution to the [Ne III] emission (as discussed in Section 7.1); these factors are likely to increase the scatter in the correlation plots. Again using a regression line fitted to the BLRG/Q objects in Figure 2 as a reference, we find that the NLRG have [O III] luminosities that are a median factor of 2.2 (mean factor 5.4 ± 1.2) lower and $L_{24\,\mu\mathrm{m}}$ that are a median factor of 1.4 (mean factor1.9 ± 1.2) lower than the BLRG/Q for a given AGN power traced by $L_{[\mathrm{Ne\,III}]}$.

Three objects are easily identifiable in Figure 2(a) with $L_{[\mathrm{O\,IV}]} < 10^{35}$ W as a group lying well below the correlation defined by the NLRG, with factors of 13, 20, and 41 lower $L_{[\mathrm{O\,III}]}$ than expected for a BLRG/Q of equivalent $L_{[\mathrm{O\,IV}]}$. One possible explanation for this result is that large-scale disk structures in the host galaxies cause enhanced dust extinction of the [O III] emission. It is notable that the host galaxies of all of these outlier objects show evidence for large-scale disks with dust lanes (3C285, Madrid et al. 2006; 3C305, Chiaberge et al. 1999; PKS1814-63, Morganti et al. 2011); they are also among the objects with the strongest H_2 detections. This H_2 emission

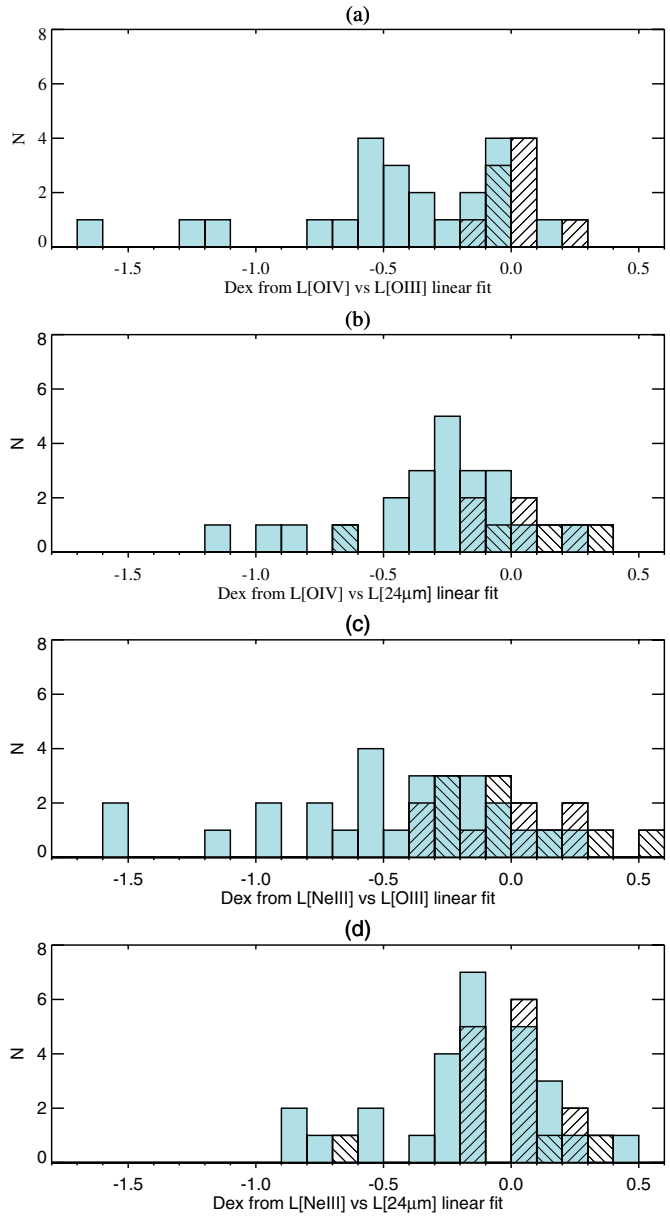

Figure 5. Plots showing the displacement of the sample objects from a regression line fitted to the BLRG/Q for the data presented in Figures 2(a) and (b) and 3(a) and (b). Crossed bars in the histograms are BLRG/Q, and filled bars are NLRG. The results are shown in dex.

(A color version of this figure is available in the online journal.)

could plausibly originate in the same dust disk described above, adding weight to this hypothesis.

5.1. Mid-infrared H_2 Emission Lines

Comprehensive studies of H_2 in radio galaxies are presented in Ogle et al. (2007, 2010), Nesvadba et al. (2010), and Guillard et al. (2012). These studies have shown that radio-loud MOHEGs have extremely high H_2/PAH ratios, indicative of jet shock excitation of H_2. We have detected H_2 lines ($S(1)$ through $S(7)$) in a minority of objects (10 out of 56, 18%; Table 4). Such H_2 lines are an indicator of shocked molecular gas as well as a tracer of the molecular gas contents of the host galaxies. It is notable that for the 2Jy sample the H_2 detections in the IRS spectra occur only in objects that also have PAH detections (Dicken et al. 2012).

The fact that H_2 and PAH are detected together suggests a link between the two emission features. Indeed, given that PAH features are known indicators of young stellar populations, the H_2 features may be tracing the total reservoir of molecular gas that fuels recent episodes of star formation in the host galaxies. However, aside from the detection statistics, we do not find a strong correlation between PAH and H_2 equivalent widths for objects in which both features are detected. This may reflect the fact that the strength of the H_2 emission depends not only on the total reservoir of molecular gas but also on how the molecular emission is excited. Indeed, Ogle et al. (2010) and Nesvadba et al. (2010) have shown that the H_2 emission is likely to be excited by shocks dissipating mechanical energy in at least two of our sample objects (3C293, 3C326). It is also important to bear in mind that PAH emission itself is not necessarily a good quantitative indicator of the star formation rates (Dicken et al. 2012).

We further note that 8 of the 10 objects with H_2 detections have relatively low redshifts $z < 0.1$, and the remaining 2 objects are both compact steep-spectrum objects that may tend toward circumnuclear gas environments that are denser/richer than more extended radio galaxies (Tadhunter et al. 2011). Because it is unlikely that we are seeing an evolutionary effect over this relatively narrow redshift range, the H_2 detections could show a preference to occur in radio galaxies that have large-scale disks; such objects are more common at lower redshifts and radio powers in the two samples. Clear examples of such disklike radio galaxies include PKS1814-63, 3C293, and 3C305 (referred to in the previous section).

6. SILICATE FEATURES AND THE MID-IR CONTINUUM

6.1. Silicate Features

Out of the 56 observed/detected objects in our study, 32 were fitted with a 10 μm silicate feature when modeling with the PAHFIT program. However, not all of these 32 objects show clear evidence for silicates based on visual inspection of the spectra. Therefore, to robustly measure the strengths of the silicate emission/absorption features we adopt the definition of Spoon et al. (2007): the silicate strength is the log ratio of the observed flux density at the center of the silicate feature and the local continuum:

$$S_{9.7} = \ln\left(\frac{F_{9.7\,\mu\mathrm{m}}[measured]}{F_{9.7\,\mu\mathrm{m}}[continuum]}\right) \quad (1)$$

where $F_{9.7\,\mu\mathrm{m}}[measured]$ and $F_{9.7\,\mu\mathrm{m}}[continuum]$ are the measured flux and the interpolated continuum flux at the center of the 9.7 μm feature, respectively; a similar expression applies to the 18 μm feature. To calculate $S_{9.7}$ and S_{18} we first subtracted the PAH features and emission lines from the spectra. Next, we measured $F_{9.7/18\,\mu\mathrm{m}}[Measured]$ using a bin width of 0.5 μm. We then calculated $F_{9.7/18\,\mu\mathrm{m}}[continuum]$ by fitting a second-order polynomial function to the continuum measured in 3 μm wide[30] bins on either side of the silicate feature and interpolating the fit to estimate the continuum level at the center of the feature at 9.7/18 μm. Uncertainties on the measured silicate strengths were calculated by combining the uncertainty in the interpolated continuum measurement and the uncertainty in the flux measured in the spectra at the center of the silicate feature. The results are presented in Tables 5 and 6, where we have indicated $>3\sigma$ silicate detections in bold. Note that for objects that

[30] Bin widths of 6–9 μm and 13–16 μm.

Table 5
2Jy Sample: Continuum Features

Name	z	Optical	Radio	$S_{9.7\,\mu m}$	±	$S_{18\,\mu m}$	±	20/7 μm
0023−26	0.322	NLRG	CSS	−0.33	± 0.15	−0.06	± 0.28	1.204
0034−01	0.073	WLRG	FRII	**0.40**	± 0.06	−0.10	± 0.03	0.476
0035−02	0.220	BLRG	(FRII)	0.02	± 0.05	0.05	± 0.04	0.617
0038+09	0.188	BLRG	FRII	**0.21**	± 0.02	0.04	± 0.02	0.598
0039−44	0.346	NLRG	FRII	**−0.09**	± 0.02	0.02	± 0.02	0.722
0043−42	0.116	WLRG	FRII	**−0.22**	± 0.02	−0.01	± 0.02	0.340
0105−16	0.400	NLRG	FRII	0.11	± 0.04	−0.12	± 0.06	0.610
0117−15	0.565	NLRG	FRII	0.01	± 0.04	0.00	± 0.03	1.044
0213−13	0.147	NLRG	FRII	**−0.37**	± 0.01	−0.01	± 0.01	0.554
0235−19	0.620	BLRG	FRII	**0.24**	± 0.02	0.01	± 0.02	0.295
0252−71	0.566	NLRG	CSS	**0.39**	± 0.07	0.04	± 0.05	1.004
0347+05	0.339	WLRG	FRII	**−0.79**	± 0.06	−0.15	± 0.07	0.275
0349−27	0.066	NLRG	FRII	0.03	± 0.02	−0.02	± 0.04	0.438
0404+03	0.089	NLRG	FRII	**−1.02**	± 0.08	−0.05	± 0.06	0.652
0409−75	0.693	NLRG	FRII	**−0.33**	± 0.08	0.10	± 0.04	2.245
0442−28	0.147	NLRG	FRII	−0.04	± 0.02	0.02	± 0.02	0.337
0620−52	0.051	WLRG	FRI	0.14	± 0.06	0.02	± 0.04	0.239
0625−35	0.055	WLRG	FRI	0.03	± 0.03	−0.02	± 0.02	0.248
0625−53	0.054	WLRG	FRII	0.20	± 0.13	0.18	± 0.14	0.103
0806−10	0.110	NLRG	FRII	**−0.33**	± 0.02	−0.03	± 0.02	0.854
0859−25	0.305	NLRG	FRII	−0.09	± 0.04	0.04	± 0.05	0.533
0915−11	0.054	WLRG	FRI	**−0.30**	± 0.04	−0.11	± 0.06	0.318
0945+07	0.086	BLRG	FRII	**0.19**	± 0.04	0.00	± 0.03	0.389
1136−13	0.554	Q	FRII	**0.21**	± 0.02	0.00	± 0.02	0.431
1151−34	0.258	Q	CSS	0.01	± 0.02	0.01	± 0.04	0.334
1306−09	0.464	NLRG	CSS	0.05	± 0.05	−0.03	± 0.10	0.462
1355−41	0.313	Q	FRII	**0.20**	± 0.02	0.02	± 0.02	0.347
1547−79	0.483	BLRG	FRII	**0.24**	± 0.04	0.01	± 0.06	0.671
1559+02	0.104	NLRG	FRII	**−0.36**	± 0.02	−0.02	± 0.01	1.281
1602+01	0.462	BLRG	FRII	**0.15**	± 0.03	−0.01	± 0.04	0.934
1648+05	0.154	WLRG	FRI	...		...		...
1733−56	0.098	BLRG	FRII	−0.03	± 0.02	0.01	± 0.02	0.461
1814−63	0.063	NLRG	CSS	**−0.31**	± 0.02	−0.05	± 0.04	0.472
1839−48	0.112	WLRG	FRI	0.21	± 0.08	−0.10	± 0.10	0.237
1932−46	0.231	BLRG	FRII	−0.25	± 0.09	0.07	± 0.17	1.184
1934−63	0.183	NLRG	GPS	0.11	± 0.04	−0.02	± 0.03	2.122
1938−15	0.452	BLRG	FRII	0.26	± 0.11	0.02	± 0.14	0.872
1949+02	0.059	NLRG	FRII	0.01	± 0.02	−0.05	± 0.02	0.606
1954−55	0.060	WLRG	FRI	0.31	± 0.11	0.01	± 0.10	0.196
2135−14	0.200	Q	FRII	...		...		...
2135−20	0.635	BLRG	CSS	**−0.51**	± 0.03	0.00	± 0.04	0.547
2211−17	0.153	WLRG	FRII	...		...		...
2221−02	0.057	BLRG	FRII	**0.23**	± 0.03	**0.05**	± 0.01	0.297
2250−41	0.310	NLRG	FRII	**−0.68**	± 0.01	−0.05	± 0.04	0.497
2314+03	0.220	NLRG	FRII	0.03	± 0.03	0.01	± 0.04	2.396
2356−61	0.096	NLRG	FRII	**−0.55**	± 0.01	−0.03	± 0.01	0.895

Notes. Table presenting basic parameters of the 2Jy sample as well as spectral continuum feature data. Definitions for Column 3 are: NLRG, narrow-line radio galaxy; BLRG/Q, broad-line radio galaxy; WLRG, weak-line radio galaxy; Q, quasar. We note that PKS0625-35 is also classified as a BL Lacertae object. Definitions for column 4 are: FRI, Fanaroff–Riley type 1 object; FRII, Fanaroff–Riley type 2 object; CSS, compact steep spectrum object; GPS, gigahertz peaked spectrum object. Columns 5 and 7 present silicate strength defined in Section 6.1, Equation (1) for 10 and 18 μm, respectively. Silicate detections (3σ) are marked in bold. Column 9 presents the spectral color 20/7 μm.

have strong PAH features that straddle the 10 μm feature (e.g., PKS2135-20; see below), the silicate strengths are likely to be less accurate because of the difficulty of accurately separating the silicate and PAH features.

Figure 6 shows a clear tendency for BLRG/Q to have silicate emission and NLRG to have silicate absorption: 10 (91%) of the 11 objects with significant silicate emission are BLRG/Q, while 18 (95%) of the 19 with significant silicate absorption are NLRG or WLRG. These results are consistent with those found in many previous studies of AGN, for example, Shi et al. 2006, investigating a mixed sample of Seyferts, quasars, and 15 radio galaxies; Hao et al. 2007, investigating Seyferts and ultra-luminous infrared galaxies (ULIRGs); Baum et al. 2010, investigating Seyferts; and Landt et al. 2010, investigating 12 radio galaxies. Our results confirm the BLRG/Q to NLRG silicate dichotomy for a large, complete sample of powerful radio galaxies at intermediate redshifts.

We further note that the x and y axes of Figure 6(a) are set to an equivalent range in silicate strength. Therefore, it is immediately noticeable that the range of the measured $S_{9.7}$ values is far greater than that of the measured S_{18} values. This

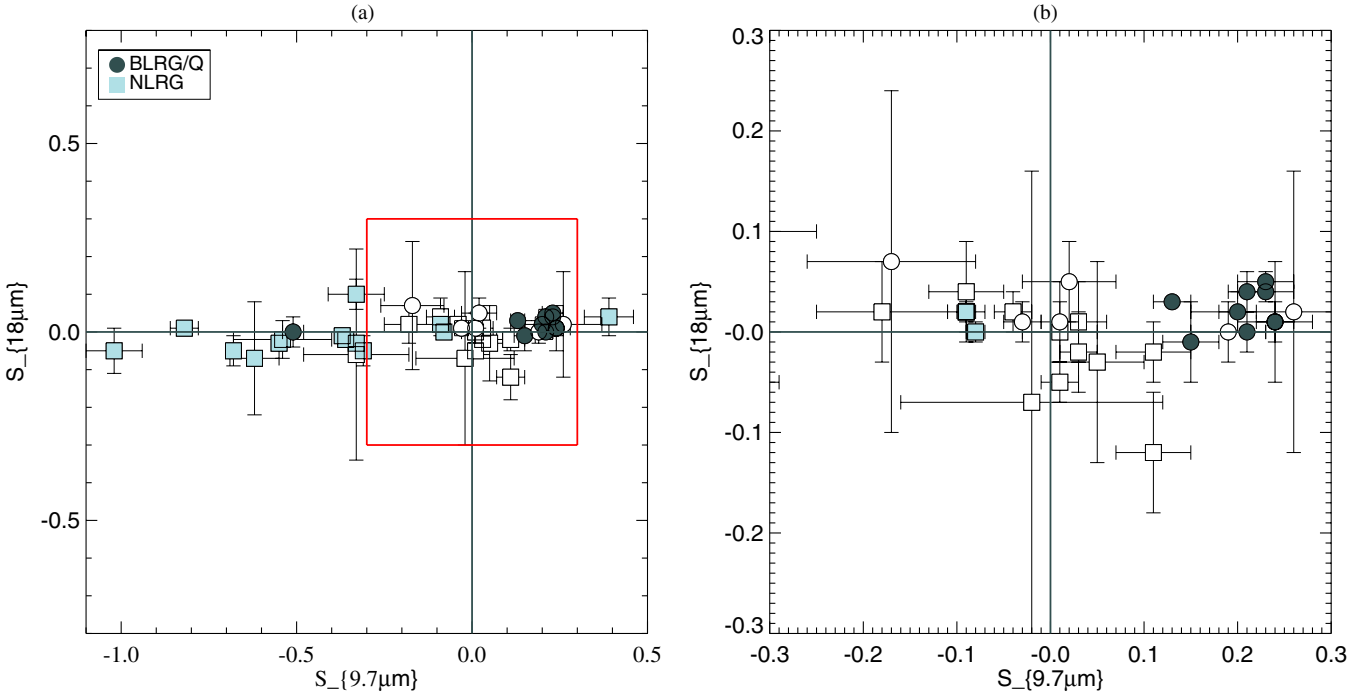

Figure 6. Plots showing $S_{9.7}$ vs. S_{18} silicate strength for the BLRG/Q and NLRG objects in the 2Jy and 3CRR samples. Filled symbols are 3σ detections; open symbols are undetected, i.e., below 3σ. Left: all objects with IRS spectra. Right: zoom of area marked with a red box in the left plot.
(A color version of this figure is available in the online journal.)

Table 6
3CRR Sample: Continuum Features

Name	z	Optical	Radio	$S_{9.7\,\mu m}$	±	$S_{18\,\mu m}$	±	20/7 μm
3C33	0.060	NLRG	FRII	**−0.08**	± 0.01	0.00	± 0.01	0.621
3C35	0.067	NLRG	FRII	...		...		...
3C98	0.030	NLRG	FRII	−0.18	± 0.07	0.02	± 0.05	0.772
3C192	0.060	NLRG	FRII	−0.02	± 0.14	−0.07	± 0.23	...
3C236	0.101	WLRG	FRII	0.10	± 0.10	0.14	± 0.13	0.782
3C277.3	0.085	WLRG	FRI/FRII	...		...		...
3C285	0.079	NLRG	FRII	**−0.54**	± 0.14	−0.02	± 0.05	1.101
3C293	0.045	WLRG	FRI/FRII	**−1.15**	± 0.03	−0.02	± 0.02	0.263
3C305	0.042	NLRG	CSS/FRII	**−0.62**	± 0.07	−0.07	± 0.15	0.828
3C321	0.096	NLRG	FRII	**−0.82**	± 0.04	0.01	± 0.01	2.659
3C326	0.090	NLRG	FRII	0.06	± 0.26	−0.02	± 0.44	0.123
3C382	0.058	BLRG	FRII	**0.23**	± 0.03	**0.04**	± 0.01	0.163
3C388	0.092	WLRG	FRII	0.23	± 0.18	0.13	± 0.20	0.192
3C390.3	0.056	BLRG	FRII	**0.13**	± 0.02	**0.03**	± 0.00	0.469
3C452	0.081	NLRG	FRII	**−0.09**	± 0.01	0.02	± 0.01	0.679
4C73.08	0.058	NLRG	FRII	...		...		...
da240	0.036	WLRG	FRII	...		...		...

Notes. Table presenting basic parameters of the 3CRR sample as well as spectral continuum feature data. Definitions are the same as Table 5.

is not surprising because, as described in Section 3.1, when applying the PAHFIT model with silicate absorption, we found a much improved fit to the objects using high ratios of 10 μm/18 μm absorption opacity.

Although in the majority of cases the measurements of the 18 μm silicate feature are consistent with zero within the uncertainties, three BLRG/Q objects (3C445, 3C382, 3C390.3) have 18 μm silicate emission detected at a $>3\sigma$ level. An emission feature at 18 μm is clearly visible in the spectra of all these objects. It is also notable that, in general, BLRG/Q with emission at 9.7 μm are fitted better with a PAHFIT model that includes the 18 μm emission feature.

It is also interesting to consider the detection rate of silicate absorption in the NLRG from the 2Jy and 3CRR samples: 56%. Given that, on the basis of the unified schemes, we expect circumnuclear dust structures to obscure the AGN in these objects, it is perhaps surprising that nearly half the NLRG in the samples show no evidence for silicate absorption. In most cases this lack of strong silicate absorption cannot be attributed to a low S/N. Rather, this result may indicate dilution of the mid-IR continuum by non-torus sources of emission. Possibilities include emission from dust in the NLR (e.g., Radomski et al. 2002) that is out of the plane of the torus and/or nonthermal synchrotron emission. However, the lack of detections may also

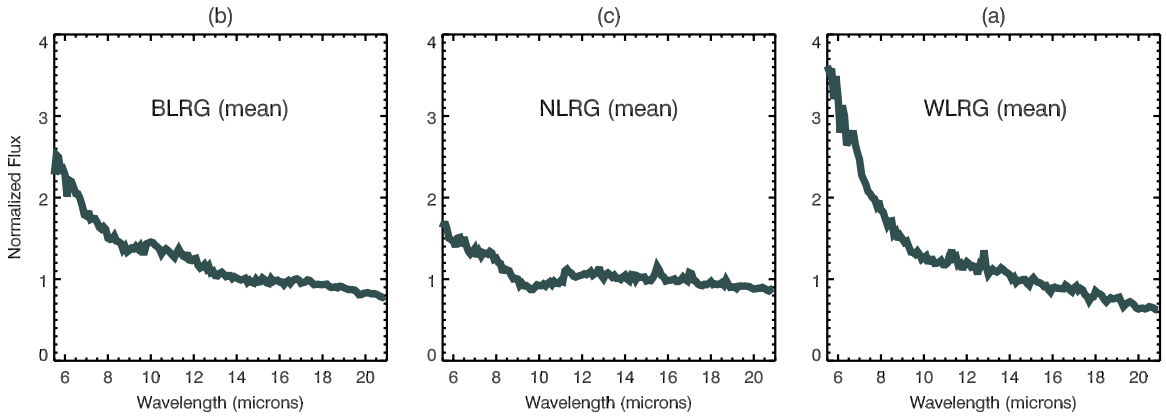

Figure 7. Mean spectra for the different optical classes in the combined 2Jy and 3CRR samples. All three spectra have been normalized so that they have the same relative flux at 14 μm.

reflect the true diversity in the mid-IR emitting dust structures and/or the range in the angle of such structures to the line of sight.

Looking at Figure 6(b), it is clear that the scatter of silicate emission values for the BLRG/Q with significant silicate emission detections[31] is much smaller than that of the silicate absorption values: whereas the measured silicate emission strengths ($S_{9.7}$) for the BLRG/Q range from 0.13 to 0.24 (i.e., a spread of 0.11), the silicate absorption strengths measured in the NLRG range from −0.09 to −1.02 (a spread of approximately 1.0). It is possible that the range of silicate absorption depths of the NLRG reflects varying lines of sight through the central obscuring dust structures or varying degrees of dilution by non-torus continuum components. However, although we expect the range of emission feature strengths to be less than that of the absorption, the narrow range of $S_{9.7}$ emission measured for the majority of BLRG/Q suggests remarkable uniformity in the mid-IR emission mechanism in such objects.

There are two notable outliers in silicate strength compared to the general trends presented above. PKS2135-20 is a BLRG with apparently strong silicate absorption. Although silicate absorption cannot be entirely ruled out for this object, the strength of the PAH features detected in its IRS spectra makes the contribution of silicate absorption difficult to accurately quantify because the PAH emission dominates the wings of the putative silicate absorption feature. In contrast, the compact steep-spectrum object PKS0252-71 has the highest $S_{9.7}$ *emission* strength measured for any object in the two samples, despite the fact that it is a NLRG; it is not clear why a NLRG should have stronger silicate emission than seen for BLRG/Q objects.

We further note that for all but one (PKS0235-19) of the objects with significant silicate emission, we find that the peak of the 9.7 μm silicate emission feature is redshifted. The wavelength range of the redshifted peak is 10.0–10.6 μm, but the shift is not seen in the 18 μm feature (where detected). Redshifts in the silicate emission feature have been measured in several other *Spitzer* studies of AGNs (e.g., Shi et al. 2006; Landt et al. 2010; Leipski et al. 2010), but there is currently no general agreement about the cause of the shift, which has been variously attributed to obscuration effects, variations in the dust grain size or dust chemistry, radiative transfer effects, or a shift in the blackbody spectrum due to temperature (Leipski et al. 2010). It is also important to note that $S_{9.7}$ emission strength may be slightly underestimated in Tables 5 and 6 because we did not allow for any shift in the peak of this feature in our measurements, and therefore, the silicate emission strength is not measured at the peak of emission.

6.2. Spectral Shape

It is interesting to consider whether there are any correlations between the overall mid-IR continuum shapes and the strengths of the silicate features. For example, in the simplest case of a screen of absorbing dust between the mid-IR continuum source and the observer, it would be expected that because of extinction effects, the continuum would become redder as the silicate absorption depth increased.

In Figure 7 we plot mean spectra divided into optical classifications. After emission line and PAH features were subtracted, the mean spectra were created by resampling the data in wavelength bins and normalizing all the spectra to have the same flux level at 20 μm. The results clearly show the silicate feature is in emission for BLRG/Q and in absorption for NLRG, but the appearance of these features in the mean spectra is likely to be a consequence of objects with strong silicate features dominating the mean and does not reflect the fact that silicate features are not detected in a significant fraction (∼40%) of the spectra of the individual objects. Looking at the overall spectral shape, the mean spectra of the three optical classes show the largest contrast toward the blue end of the spectrum, in particular the mean spectrum of the WLRG. This can be attributed to the stellar contribution from the host galaxies, which is likely to dominate the short-wavelength continuum for these nearby objects, which have weaker AGNs. However, the mid-IR continuum shape of the BLRG/Q is also notably bluer than that of the NLRG, as expected if the latter objects are affected by a higher level of dust extinction.

To further investigate the mid-IR continuum shapes, we have measured the 20/7 μm continuum colors from the spectra of individual objects, following the subtraction of all emission lines, PAH, and silicate features using the PAHFIT model. Figure 8 shows the 20/7 μm color plotted against the 9.7 μm silicate strength ($S_{9.7}$). Although some of the BLRG/Q objects with the strongest 9.7 μm emission features also have the bluest 20/7 μm colors and some of the NLRG with the strongest 9.7 μm absorption features have the reddest colors, overall, the

[31] Note the BLRG/Q without silicate detection have either strong PAH features (PKS1151-34, PKS1733-56, PKS2135-20) that can mask the emission feature, noisy spectra (PKS1938-15), or calibration uncertainties (PKS0035-02).

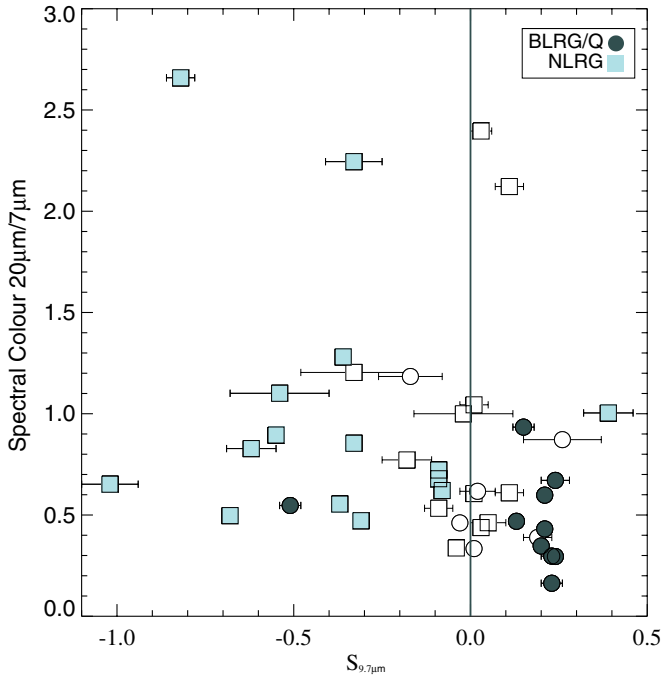

Figure 8. Plot of $S_{9.7}$ vs. IRS 20/7 μm spectral color. Filled squares are narrow-line radio galaxies; filled circles are broad-line radio galaxies and quasars. Unfilled symbols represent objects that are undetected in $S_{9.7}$, i.e., below 3σ.

(A color version of this figure is available in the online journal.)

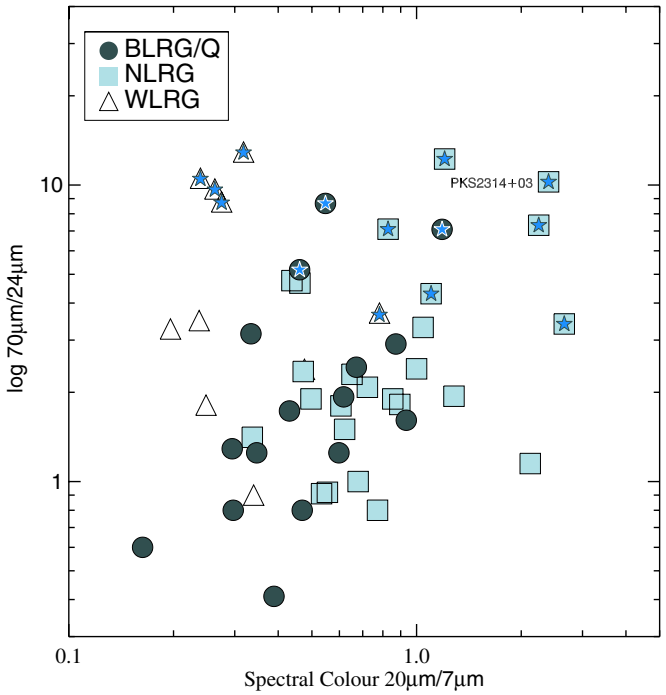

Figure 9. Plot of the IRS spectral color (7 μm/20 μm) vs. mid- to far-infrared color (70 μm/24 μm). Filled squares are narrow-line radio galaxies; filled circles are broad-line radio galaxies and quasars; open triangles are weak-line radio galaxies. In addition, objects with evidence for recent star formation activity are indicated with a blue star.

(A color version of this figure is available in the online journal.)

plot shows a large scatter (see also Ogle et al. 2006). This lack of a clear-cut correlation between the silicate feature strength and the mid-IR color argues against the naive expectations of a simple dust screen extinction model.

One possible reason for the lack of a correlation in Figure 8 is that non-torus emission components contribute to the mid-IR continuum. Along with the possibility of the NLR emission components discussed in Section 6.1, starburst-heated dust may also contribute to the longer-wavelength mid-IR emission. In order to investigate the significance of the latter, in Figure 9 we plot 20/7 μm versus MFIR color (70/24 μm; measured from *Spitzer*/MIPS photometric data; Dicken et al. 2010). Once again, we have labeled the objects according to optical class; in addition, we have indicated objects that show good, independent evidence for recent star formation activity (RSFA) at optical and mid-IR wavelengths, as defined in Dicken et al. (2012). Figure 9 shows that 70/24 μm color ratio is an excellent indicator of RSFA (see also Dicken et al. 2009, 2012). However, this plot does not reveal any clear relationship between the shape of the mid-IR spectrum and the presence of RSFA for the sample as a whole, apart from the fact that three-fourths of the objects with extremely red 20/7 μm colors also show evidence for RSFA and have red starburst-like 70/24 μm MFIR colors. One of the latter objects, the ULIRG PKS2314+03 (identified in Figure 9), has unusually red mid-IR and MFIR continuum colors, and this result is paralleled in Figure 2(b), where PKS2314+03 stands out as the only NLRG lying above the correlation between $L_{[\mathrm{O\,IV}]}$ and $L_{24\,\mu\mathrm{m}}$. Therefore, it is probable that the RSFA in PKS2314+03 is making a significant contribution to its 24 μm emission. Overall, while the presence of RSFA is likely to increase the scatter in the mid-IR colors, it is unlikely to provide the full explanation for the lack of correlation in Figure 8, since the overwhelming majority (>65%) of objects in our samples show no evidence for significant RSFA (Dicken et al. 2012).

7. DISCUSSION

7.1. Origin of the Mid-IR Emission Lines

The higher-ionization fine-structure lines investigated so far (e.g., [O IV]: $E_{\mathrm{ion}} = 54.9$ eV; [Ne III]: $E_{\mathrm{ion}} = 41.0$ eV) not only are thought to originate predominantly from the narrow-line regions of AGNs (Meléndez et al. 2008; Rigby et al. 2009; Diamond-Stanic et al. 2009) but are also fainter in pure starburst galaxies, where they can only arise from shocks associated with very hot stars (Lutz et al. 1998). In contrast, the lower-ionization fine-structure lines ($E_{\mathrm{ion}} \leqslant 30$ eV) can be readily produced by stellar photoionization in H II regions rather than by AGNs. Indeed, previous studies used the relative strength of the high- and low-ionization lines to gauge the relative dominance of starburst and AGN in Seyfert and ULIRG objects (e.g., Sturm et al. 2002; Veilleux et al. 2009). Because optical line ratios become unreliable for heavily obscured objects, mid-IR diagnostics are an important alternative for determining the dominant ionization mechanism.

Out of the 56 observed/detected objects in the 2Jy and 3CRR samples we detect [Ne II] λ12.81 μm ($E_{\mathrm{ion}} = 21.6$ eV) in 39 objects (70%). This line has the second lowest ionization energy among the mid-IR fine-structure lines detected and presented in this work, the lowest being the weaker [Ar III] λ6.98 μm line ($E_{\mathrm{ion}} = 15.8$ eV), which suffers from a much lower detection rate (15/56, 27%).

To further investigate the origin of the mid-IR lines in Figure 10, we plot $L_{[\mathrm{Ne\,II}]}$ versus $L_{[\mathrm{O\,IV}]}$ and $L_{[\mathrm{Ne\,III}]}$, including both the strong-line and weak-line radio galaxies and again identifying objects with evidence for RSFA at optical and mid-IR wavelengths.

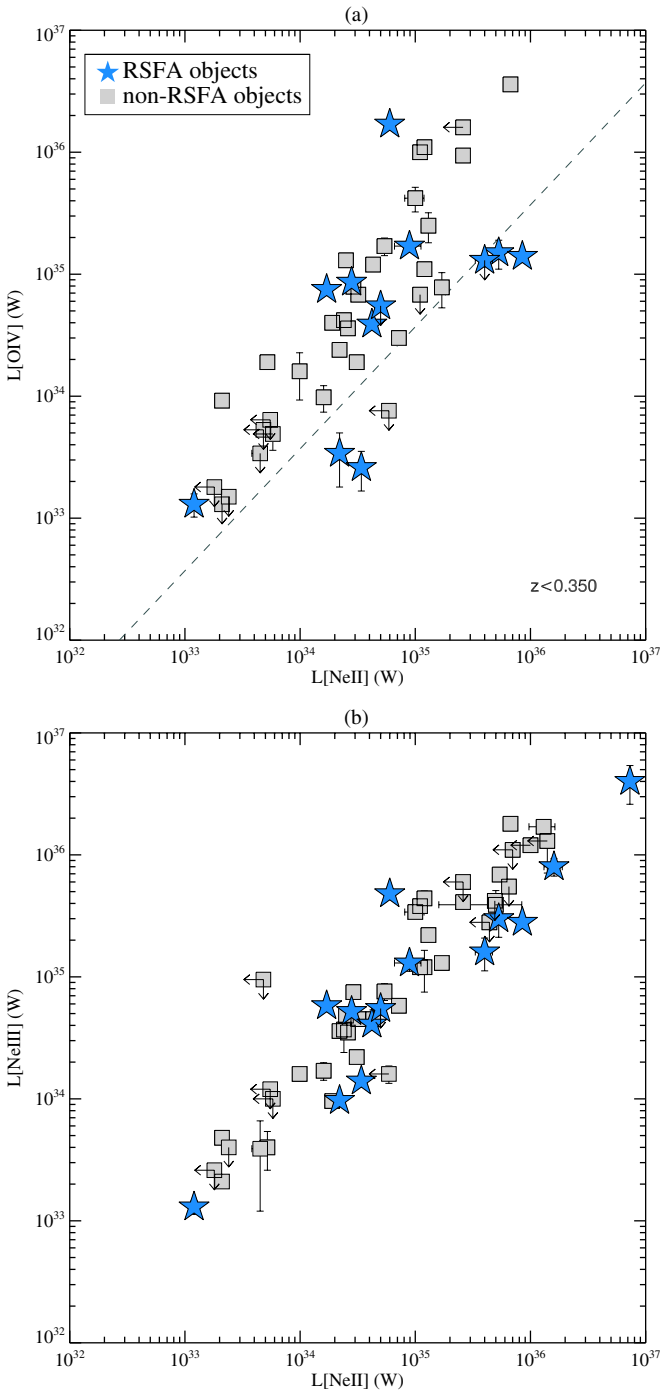

Figure 10. Plots of $L_{[\mathrm{Ne\,II}]}$ vs. $L_{[\mathrm{O\,IV}]}$ and $L_{[\mathrm{Ne\,III}]}$ with objects identified with recent star formation activity (RSFA) marked as stars. These plots include strong-line and weak-line objects. The line plotted in (a) represents the critical line ratio ([Ne II]/[O IV] = 2.7) that marks the boundary between AGN and starburst origin for the infrared emission lines. Objects below this line are expected to have a star formation origin.

(A color version of this figure is available in the online journal.)

Studying Figures 10(a) and (b), both $L_{[\mathrm{O\,IV}]}$ and $L_{[\mathrm{Ne\,III}]}$ appear to correlate well with $L_{[\mathrm{Ne\,II}]}$. Given the evidence presented in this paper for an AGN origin of both the [O IV] and [Ne III] emission lines, it follows that the [Ne II] emission line is also likely to have an AGN origin in most objects. However, mid-IR lines such as [Ne II] have been shown to be produced predominantly by star formation in studies of Seyfert galaxies (e.g., Veilleux et al. 2009); therefore, we should consider the possibility that star formation contributes to this emission line. In fact, it is notable that $L_{[\mathrm{Ne\,II}]}$ is detected in all but one[32] of the RSFA identified objects.

Considering Figure 10(a), the three RSFA objects with the highest $L_{[\mathrm{Ne\,II}]}$ luminosities, lying in a small group below the apparent correlation (PKS0023-26, PKS0347+05, and PKS2314+03), all have red mid-infrared spectral continuum colors and the *coolest* 70/24 μm colors as well as strong PAH features. Moreover, the two RSFA identified objects that fall below the apparent correlation toward the center of Figure 10(a), are the weak-line objects PKS0915-11 (Hydra A) and 3C293. These two objects have similar IRS spectra, showing weak continua at longer mid-IR wavelengths, very strong PAH features, and high equivalent width [Ne II] emission. They also show high equivalent width detections of the low-ionization emission line [Ar III] λ6.98 μm.

On the basis of a study of well-known nearby Seyfert objects, Sturm et al. (2002) proposed that objects with values of the [Ne II]/[O IV] ratio lower than or equal to 2.7 are likely to have a dominant AGN origin, whereas those with higher ratios are likely to have a significant contribution from starburst heating. We have plotted the line that represents the critical ratio in Figure 10(a). Considering the [Ne II]/[O IV] ratio for the combined 2Jy and 3CRR sample,[33] the majority of objects have [Ne II]/[O IV] ratios below 2.7, and the mean is [Ne II]/[O IV] = 0.70 ± 0.63 for the non-RSFA sample. This supports an AGN origin for the mid-IR emission lines in the majority of the radio galaxies in the combined sample. However, the five RSFA objects lying below the correlation in Figure 10(a), mentioned above, all have [Ne II]/[O IV] > 2.7. Given the independent evidence for these five objects to have the strongest RSFA in our samples, the [Ne II]/[O IV] ratio proves to be an effective diagnostic to gauge dominant star formation activity in powerful radio galaxies.

Returning to Figure 10(b), which plots $L_{[\mathrm{Ne\,II}]}$ against $L_{[\mathrm{Ne\,III}]}$, it is interesting that, although many of the RSFA objects lie at the bottom edge of the apparent correlation, there are no objects that show high ratios of [Ne II]/[Ne III] and fall well below the correlation, seen in Figure 10(a) for the [Ne II]/[O IV] ratio; it is also clear that the degree of scatter is lower in the $L_{[\mathrm{Ne\,II}]}$ versus $L_{[\mathrm{Ne\,III}]}$ plot. These results can be explained if star formation makes a significant contribution to the [Ne III] emission, as well as the [Ne II] emission, thus reducing the usefulness of the [Ne II]/[Ne III] ratio as a useful AGN or star formation diagnostic. This explanation is also consistent with the results from Section 5, which show that $L_{[\mathrm{Ne\,III}]}$ is not as reliable a tracer of AGN power as $L_{[\mathrm{O\,IV}]}$.

In summary, a maximum of 35% of the powerful radio galaxies show evidence for RSFA, and even fewer (8%) show evidence that the star formation activity contributes significantly to the production of the mid-IR emission lines. It is therefore likely that for the majority of powerful radio galaxies, both the high- and low-ionization mid-IR lines are dominated by AGN photoionization. On the other hand, it is clearly important to be cautious about using the [Ne III] and particularly the [Ne II]

[32] 3C236, which has the lowest equivalent width detection of the star formation tracing PAH and second warmest color ratio (70/24 μm = 3.4) of all the RSFA objects.

[33] Two RSFA objects (PKS2135-20; PKS0409-75) could not be included in this analysis because of their [O IV] emission line being redshifted out of the rest wavelength range of the spectra.

fine-structure lines as indicators of AGN power in objects that show independent evidence for RSFA.

7.2. Unification

The idea of an orientation-based unified scheme for the optical classes of radio sources was proposed over two decades ago (e.g., Barthel 1989), with the BLRG/Q proposed to represent a population with the torus axis oriented close to the line of sight, allowing a full view of the broad line and continuum emitting regions, and the NLRG to represent a heavily obscured population in which the axis of the torus is oriented at a large angle to the line of sight. Optical polarization studies of radio-loud AGNs have provided the evidence that NLRG and BLRG/Q indeed represent the same population viewed from different directions (e.g., Antonucci 1984; Cohen et al. 1999). Mid-infrared spectra are ideal for further testing such unified schemes because the emission is less likely to suffer from obscuration compared to optical wavelength studies. Following previous investigations of unification using IRS spectra (e.g., Ogle et al. 2006; Shi et al. 2006; Leipski et al. 2009), with the new 2Jy sample IRS data and the extensive archive of complementary multiwavelength data for this sample, we are able to further test the orientation-based unified schemes.

We have presented evidence that the degree of NLR extinction at optical wavelengths depends on the classifications of the sources, albeit mildly and with a wide dispersion. Median ratio values for the two optical classes of radio sources in the combined sample are [O III]/[O IV] = 1.6 (BLRG/Q) and 0.7 (NLRG); similar results have been found for type 1 and type 2 Seyfert galaxies (e.g., Baum et al. 2010; LaMassa et al. 2010). For Seyfert type 1 and 2 galaxies LaMassa et al. (2010) also investigated [O III]/[O IV] and found a difference of a factor of 2, on average, between the [O III] luminosities of type 1 and type 2 objects, in good agreement with our results. In a previous study of radio galaxies, Haas et al. (2005) found evidence for a larger average difference, with the [O III]/[O IV] ratio a factor of approximately 10 lower for the NLRG compared with the BLRG/Q in their sample. In contrast, although there is large dispersion, our data show a median ratio between BLRG/Q and NLRG [O III]/[O IV] values of only 2.3. However, the sample of Haas et al. (2005) was statistically much smaller than that used in this study, comprising only seven NLRG and seven quasars, matched in radio luminosity.

Cleary et al. (2007) also investigated the mid-IR properties of 3CR radio galaxies and quasars at intermediate redshifts and present evidence for a difference in rest frame 15 μm luminosity. They found a difference of a factor of 2 between the mean $R_{dr} = \nu L_\nu(\mathrm{IR})/\nu L_\nu(178\ \mathrm{MHz})$ for narrow-line radio galaxies and quasars, when corrected for nonthermal contamination. They attribute this to obscuration of the mid-IR continuum emission. Despite the fact that there is an uncertainty in the R_{dr} value due to the variation in $L_{(178\ \mathrm{MHz})}$ as described in Section 4, the implied level of attenuation of the mid-IR continuum is similar to that deduced in this study on the basis of the 24/[O IV] ratio.

The evidence for obscuration and dependence on orientation of the optical classes of radio galaxies is also supported by the clear divide between detections of BLRG/Q with silicate emission and NLRG with silicate absorption. This result is well established for the Seyfert AGN population and is also predicted by clumpy torus models (Nenkova et al. 2002, 2008), where silicate emission in BLRG/Q is associated with hot dust close to the active nucleus, and the silicate absorption in NLRG is due to circumnuclear dust that absorbs the AGN continuum along certain lines of sight.

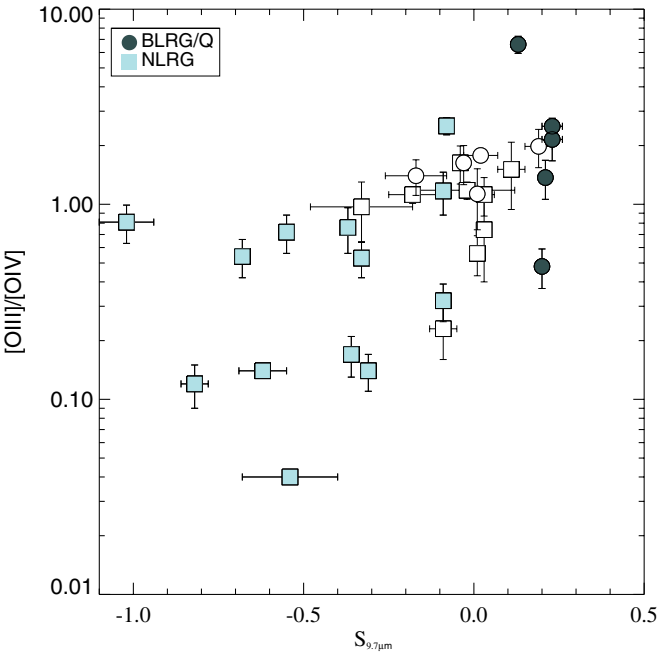

Figure 11. Plot of $S_{9.7}$ vs. [O III]/[O IV]. Filled squares are narrow-line radio galaxies; filled circles are broad-line radio galaxies. Unfilled objects are undetected in $S_{9.7}$, i.e., below 3σ.

(A color version of this figure is available in the online journal.)

In Figure 11 we investigate the possibility that objects showing evidence for attenuation of the [O III] optical emission line also show silicate absorption. We emphasize that a correlation is not necessarily expected because of the potential contamination of the mid-IR continuum by various non-torus continuum components and significant variations in the structure of the circumnuclear dust structures from object to object. Also, the [O III]/[O IV] ratio will depend on the ionization state of the gas and any differences in density, radial gas distribution, and metallicity. However, despite the scatter, a weak trend toward stronger silicate absorption for low ratios of [O III]/[O IV] can be identified. This adds weight to the hypothesis that obscuration is the main cause of the difference seen between the [O III] luminosities of NLRG and BLRG/Q.

A prediction of clumpy torus models is that the silicate absorption should be relatively shallow, with $S_{9.7} > -1.0$ (Nenkova et al. 2008). This is entirely consistent with our results. However, in addition to the relatively shallow absorption features, the detection rate of silicate absorption features in only 56% for the 9.7 μm feature and zero for the 18 μm feature. The lack of detections of silicate absorption features in >40% of the NLRG is all the more surprising given that the kiloparsec-scale disks may contribute to the measured silicate absorption over and above that produced by a compact torus structure. Gallimore et al. (2010) also found evidence that strong silicate features are not ubiquitous in AGNs: for 35% of the Seyfert galaxies in their sample the 9.7 μm feature is not detected at greater than 3σ. They found that objects without silicate detections tend to belong to particular subsamples of the Seyfert population, including Seyfert 2 objects without evidence for hidden broad-line regions, intermediate Seyfert types (S1.8-1.9), and LINERs. We find no trend in the 2Jy and 3CRR samples between silicate detection or strength and either the object classifications or their properties.

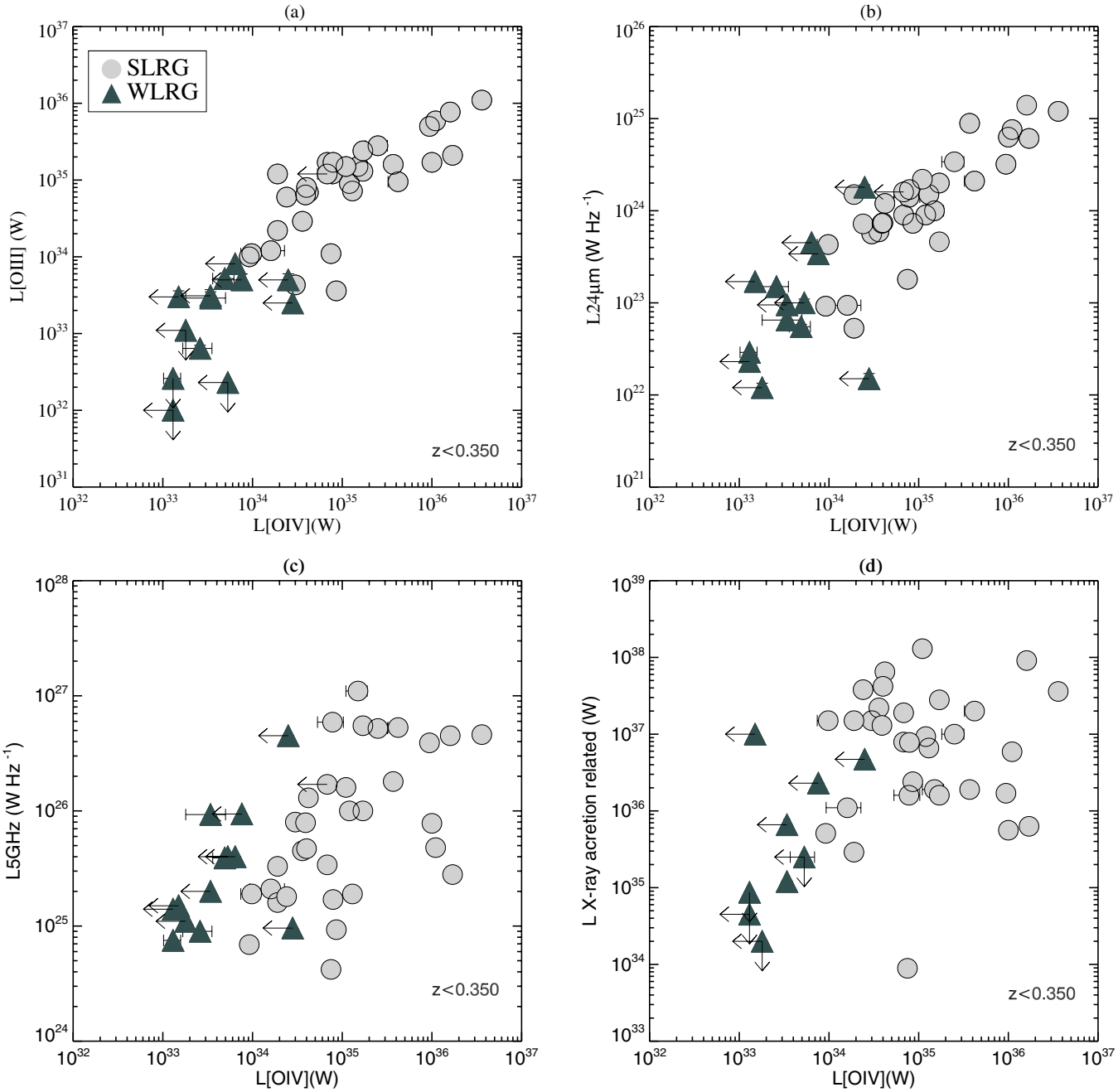

Figure 12. Plot showing $L_{[\mathrm{O\,IV}]\,\lambda 25.89\,\mu\mathrm{m}}$ vs. $L_{[\mathrm{O\,III}]\,\lambda 5007}$, $L_{24\,\mu\mathrm{m}}$, $L_{5\,\mathrm{GHz}}$, and $L_{[\mathrm{Ne\,III}]\,\lambda 15.56\,\mu\mathrm{m}}$ with objects identified as strong-line radio galaxies (SLRG) or weak-line radio galaxies (WLRG). The objects plotted are limited to objects with $z < 0.350$ because of the [O IV] line redshifted out of the redshift range of *Spitzer*/IRS. SLRG: strong-line radio galaxies/quasars.

Models predict that clumpy tori with low average numbers of clouds along the line of sight ($N_0 \leqslant 2$) never produce an absorption feature, regardless of the orientation, and that the silicate features commonly detected in Seyfert spectra are reproduced by models that include $N_0 \geqslant 5$ clouds (Nenkova et al. 2008; Alonso-Herrero et al. 2011). Overall, if we assume that the mid-IR continuum is solely due to the torus, the silicate emission (BLRG/Q) and absorption (NLRG) strengths measured in our sample are consistent with clumpy models that have relatively few clouds along the line of sight $2 < N_0 < 5$. However, the large number of nondetections of silicate absorption features is also consistent with the idea that much of the mid-IR continuum does not suffer extinction by the torus because it is emitted by structures on larger scales such as the NLR, circumnuclear starbursts, or synchrotron-emitting jets.

7.3. Weak-line Radio Galaxies

In terms of the classification of radio-loud AGNs, there has recently been much debate about the nature of WLRG and how they relate to strong-line (NLRG and BLRG/Q) objects of similar radio power (e.g., Hardcastle et al. 2007; Buttiglione et al. 2010; Smolčć & Riechers 2011). One explanation for the relatively low emission line luminosities of WLRG is that their AGNs have intrinsically low radiative powers and therefore do not produce luminous, high-ionization emission line regions by illuminating the ISM in the host galaxies, as is assumed

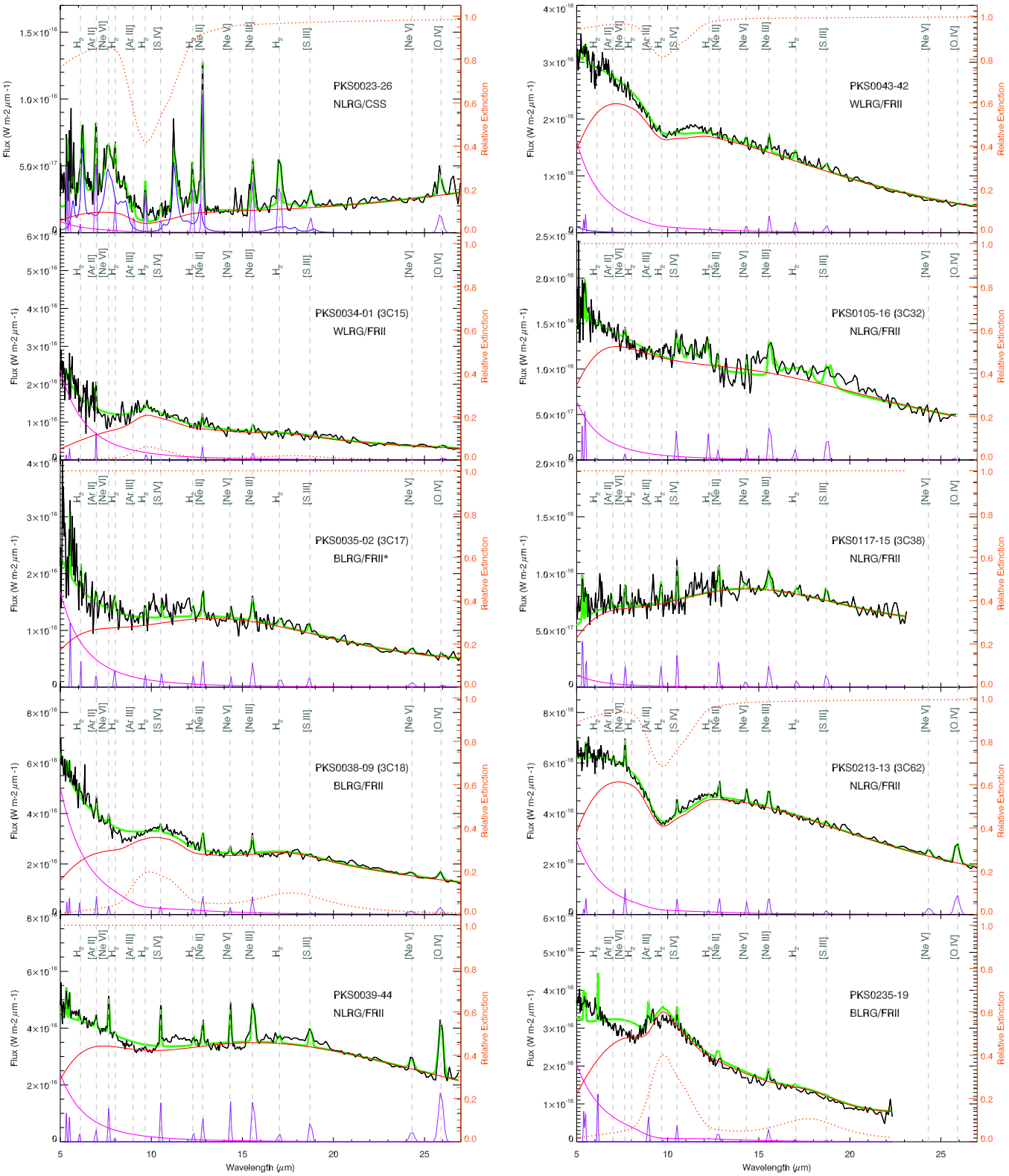

Figure 13. PAHFIT fits to the *Spitzer*/IRS spectra for the 2Jy sample. Note that all spectra were previously published in Dicken et al. (2012) and four spectra were first published in Ogle et al. (2006) and Leipski et al. (2009). Common fine-structure and H_2 emission lines are indicated by vertical gray dashed lines. The dotted orange line shows the extinction ($e^{-\tau\nu} = 1$ if there is no extinction). Prominent PAH features are indicated by the blue line. Note that data for PKS0034-01 and PKS0035-02 potentially suffer from enhanced flux calibration uncertainties at short wavelengths due to saturation of the peak-up detector (see Dicken et al. 2012 for details). The SL continuum agreement between nod positions is not good for PKS0039-44 in the range 10–14 μm, likely leading to the strange shape of the spectrum. 3C15 is also published in Leipski et al. (2009).

(An extended, color version of this figure is available in the online journal.)

to happen in strong-line radio galaxies (SLRG). Alternatively, it has been proposed that the relatively low emission line luminosities of the WLRG are due to an unusually high level of dust extinction affecting the NLR.

Dicken et al. (2009, 2010) and Hardcastle et al. (2009) showed that the WLRG have not only low [O III] emission line luminosities but also low 24 μm continuum luminosities. This already suggests that WLRG are unlikely to harbor luminous quasar-like nuclei that are obscured by dust at optical wavelengths, as also supported by the study of Ogle et al. (2006). However, as we have already seen in this study, the 24 μm emission can itself suffer from significant extinction by the circumnuclear dust; if such obscuration is particularly extreme in the WLRG compared with their SLRG counterparts, this could potentially explain the lower 24 μm luminosities of the WLRG.

We can reconsider this question using the new mid-IR emission line data. Figure 12 again shows the correlations between the AGN power indicators, but now including the WLRG plotted alongside the SLRG. Inspecting Figure 12, it is clear that the WLRG fall at the low-luminosity end of all the correlations and make up the majority of the objects with upper limits in [O IV]. The low detection rate of the WLRG using this mid-IR AGN power proxy (only 16%) reinforces our previous conclusion that WLRG have intrinsically low-power AGNs; since the [O IV] emission suffers relatively little from the effects of dust extinction compared to the optical [O III] line, these results strongly reinforce the idea that the WLRG have intrinsically low radiative powers.

8. CONCLUSIONS

We have investigated deep *Spitzer*/IRS spectra for complete samples of 46 2Jy radio galaxies ($0.05 < z < 0.7$) and 17 3CRR FRII radio galaxies ($z < 0.1$). Our main conclusions are as follows.

1. The luminosity of the mid-IR [O IV] λ25.89 μm emission line is at least as reliable a tracer of AGN power as the optical [O III] λ5007 emission line and 24 μm mid-IR continuum luminosities but has the added notable advantage that it suffers less from dust extinction. However, total radio power (at 5 GHz) and X-ray luminosity do not perform as well when compared with mid-IR [O IV] λ25.89 μm and optical [O III] λ5007 emission line luminosities as proxies of AGN power for powerful radio galaxies.
2. On the basis of comparisons between the BLRG/Q and NLRG objects in correlation plots that include the mid-IR fine-structure lines ([O IV] λ25.89 μm and [Ne III] λ15.56 μm), the optical [O III] λ5007 line emission, and the mid-IR 24 μm continuum emission both show evidence for a mild degree of attenuation of a factor of $\approx$2. We attribute this to obscuration by circumnuclear dust structures. However, the degree of attenuation is considerably lower than claimed in some previous studies of powerful radio galaxies.
3. The 10 μm silicate features are detected in approximately 60% of the objects and therefore do not appear to be ubiquitous in powerful radio galaxies. Silicate emission is predominantly detected in BLRG/Q, with a detection rate of 59%, whereas silicate absorption is only detected in NLRG, with a detection rate of 56%. This dependence on optical classification is consistent with many previous investigations of AGNs. We find no obvious relationship between silicate detection or nondetection and any other observable properties from the two samples.
4. From an analysis of the ratios of mid-IR emission lines we conclude that these lines are produced by AGN photoionization in the majority of powerful radio galaxies. However, in the small minority of objects with evidence for the strong star formation activity, stellar photoionization can make a significant contribution to the lower-ionization mid-IR emission lines (e.g., [Ne II] λ12.81 μm and [Ne III] λ15.56 μm).
5. Using the isotropic [O IV] emission line as an AGN power indicator, we provide further evidence against the idea that weak-line radio galaxies harbor intrinsically powerful, but heavily extinguished, AGNs.

We thank our friend and collaborator, the late David Axon, for all the support he gave to this project over the years. We thank the anonymous referee for useful comments, which aided this investigation and helped put the work in context. We would like to thank Jack Gallimore for assistance with the modification of PAHFIT. This work is based (in part) on observations made with the *Spitzer Space Telescope*, which is operated by the Jet Propulsion Laboratory, California Institute of Technology, under a contract with NASA. This work is also based on observations made with ESO telescopes at the Paranal Observatory. D.D. acknowledges support from a NASA grant based on observations from *Spitzer* program 50588 and the NASA ROSES ADAP program. C.R.A. is supported by a Marie Curie Intra-European Fellowship within the 7th European Community Framework Programme (PIEF-GA-2012-327934) and by the Spanish Ministry of Science and Innovation (MICINN) through project PN AYA2010-21887-C04.04. M.B.N.K. was supported by the Peter and Patricia Gruber Foundation through the PPGF fellowship, by the Peking University One Hundred Talent Fund (985), and by the National Natural Science Foundation of China (grants 11010237, 11050110414, 11173004). This publication was made possible through the support of a grant from the John Templeton Foundation and National Astronomical Observatories of the Chinese Academy of Sciences. The opinions expressed in this publication are those of the author(s) and do not necessarily reflect the views of the John Templeton Foundation or National Astronomical Observatories of the Chinese Academy of Sciences. The funds from John Templeton Foundation were awarded in a grant to The University of Chicago, which also managed the program in conjunction with National Astronomical Observatories, Chinese Academy of Sciences.

Facility: Spitzer (IRS)

REFERENCES

Alonso-Herrero, A., Ramos Almeida, C., Mason, R., et al. 2011, ApJ, 736, 82
Antonucci, R. R. J. 1984, ApJ, 278, 499
Baldi, R. D., Capetti, A., Buttiglione, S., et al. 2013, A&A, 560, A81
Barthel, P. D. 1989, ApJ, 336, 606
Barthel, P. D., & Arnaud, K. A. 1996, MNRAS, 283, L45
Baum, S. A., Gallimore, J. F., O'Dea, C. P., et al. 2010, ApJ, 710, 289
Blandford, R. D., & Znajek, R. L. 1977, MNRAS, 179, 433
Buttiglione, S., Capetti, A., Celotti, A., et al. 2009, A&A, 495, 1033
Buttiglione, S., Capetti, A., Celotti, A., et al. 2010, A&A, 509, A6
Chiaberge, M., Capetti, A., & Celotti, A. 1999, A&A, 349, 77
Cleary, K., Lawrence, C. R., Marshall, J. A., Hao, L., & Meier, D. 2007, ApJ, 660, 117
Cohen, M. H., Ogle, P. M., Tran, H. D., Goodrich, R. W., & Miller, J. S. 1999, AJ, 118, 1963
Diamond-Stanic, A. M., Rieke, G. H., & Rigby, J. R. 2009, ApJ, 698, 623

Dicken, D., Tadhunter, C., Axon, D., et al. 2009, ApJ, 694, 268
Dicken, D., Tadhunter, C., Axon, D., et al. 2010, ApJ, 722, 1333
Dicken, D., Tadhunter, C., Axon, D., et al. 2012, ApJ, 745, 172
Dicken, D., Tadhunter, C., Morganti, R., et al. 2008, ApJ, 678, 712
Draine, B. T. 2003, ARA&A, 41, 241
Gallimore, J. F., Yzaguirre, A., Jakoboski, J., et al. 2010, ApJS, 187, 172
Guillard, P., Ogle, P. M., Emonts, B. H. C., et al. 2012, ApJ, 747, 95
Gurkan, G., Hardcastle, M. J., & Jarvis, M. J. 2013, MNRAS, 438, 1149
Haas, M., Siebenmorgen, R., Schulz, B., Krügel, E., & Chini, R. 2005, A&A, 442, L39
Hao, L., Spoon, H. W. W., Sloan, G. C., et al. 2005, ApJL, 625, L75
Hao, L., Weedman, D. W., Spoon, H. W. W., et al. 2007, ApJL, 655, L77
Hardcastle, M. J., Evans, D. A., & Croston, J. H. 2007, MNRAS, 376, 1849
Hardcastle, M. J., Evans, D. A., & Croston, J. H. 2009, MNRAS, 396, 1929
Hardcastle, M. J., & Krause, M. G. H. 2013, MNRAS, 430, 174
Hes, R., Barthel, P. D., & Hoekstra, H. 1995, A&A, 303, 8
Higdon, S. J. U., Devost, D., Higdon, J. L., et al. 2004, PASP, 116, 975
Holt, J., Tadhunter, C. N., González Delgado, R. M., et al. 2007, MNRAS, 381, 611
Houck, J. R., Roellig, T. L., Van Cleve, J., et al. 2004, Proc. SPIE, 5487, 62
Inskip, K. J., Tadhunter, C. N., Dicken, D., et al. 2007, MNRAS, 382, 95
Inskip, K. J., Tadhunter, C. N., Morganti, R., et al. 2010, MNRAS, 407, 1739
Isobe, T., Feigelson, E. D., & Nelson, P. I. 1986, ApJ, 306, 490
Jackson, N., & Browne, I. W. A. 1990, Natur, 343, 43
Kemper, F., Vriend, W. J., & Tielens, A. G. G. M. 2004, ApJ, 609, 826
Laing, R. A., Riley, J. M., & Longair, M. S. 1983, MNRAS, 204, 151
LaMassa, S. M., Heckman, T. M., Ptak, A., et al. 2010, ApJ, 720, 786
Landt, H., Buchanan, C. L., & Barmby, P. 2010, MNRAS, 408, 1982
Lavalley, M., Isobe, T., & Feigelson, E. 1992, in ASP Conf. Ser. 25, Astronomical Data Analysis Software and Systems I, ed. D. M. Worrall, C. Biemesderfer, & J. Barnes (San Francisco, CA: ASP), 245
Lawrence, A., & Elvis, M. 2010, ApJ, 714, 561
Lebouteiller, V., Bernard-Salas, J., Sloan, G. C., & Barry, D. J. 2010, PASP, 122, 231
Leipski, C., Antonucci, R., Ogle, P., & Whysong, D. 2009, ApJ, 701, 891
Leipski, C., Haas, M., Willner, S. P., et al. 2010, ApJ, 717, 766
Lutz, D., Kunze, D., Spoon, H. W. W., & Thornley, M. D. 1998, A&A, 333, L75
Madrid, J. P., Chiaberge, M., Floyd, D., et al. 2006, ApJS, 164, 307
Mason, R. E., Levenson, N. A., Shi, Y., et al. 2009, ApJL, 693, L136
Mathis, J. S. 1990, ARA&A, 28, 37
Meléndez, M., Kraemer, S. B., Armentrout, B. K., et al. 2008, ApJ, 682, 94
Mingo, B., Hardcastle, M. J., Croston, J. H., et al. 2013, MNRAS, 440, 269
Morganti, R., Holt, J., Tadhunter, C., et al. 2011, A&A, 535, A97
Morganti, R., Killeen, N. E. B., & Tadhunter, C. N. 1993, MNRAS, 263, 1023
Morganti, R., Oosterloo, T., Tadhunter, C. N., et al. 1999, A&AS, 140, 355
Morganti, R., Oosterloo, T. A., Reynolds, J. E., Tadhunter, C. N., & Migenes, V. 1997, MNRAS, 284, 541
Nenkova, M., Ivezić, Ž., & Elitzur, M. 2002, ApJL, 570, L9
Nenkova, M., Sirocky, M. M., Nikutta, R., Ivezić, Ž., & Elitzur, M. 2008, ApJ, 685, 160
Nesvadba, N. P. H., Boulanger, F., Salomé, P., et al. 2010, A&A, 521, A65
Nikutta, R., Elitzur, M., & Lacy, M. 2009, ApJ, 707, 1550
Ogle, P., Antonucci, R., Appleton, P. N., & Whysong, D. 2007, ApJ, 668, 699
Ogle, P., Boulanger, F., Guillard, P., et al. 2010, ApJ, 724, 1193
Ogle, P., Whysong, D., & Antonucci, R. 2006, ApJ, 647, 161
Punsly, B., & Coroniti, F. V. 1990, ApJ, 354, 583
Radomski, J. T., Piña, R. K., Packham, C., Telesco, C. M., & Tadhunter, C. N. 2002, ApJ, 566, 675
Ramos Almeida, C., Bessiere, P. S., Tadhunter, C., et al. 2013, MNRAS, 436, 997
Ramos Almeida, C., Bessiere, P. S., Tadhunter, C. N., et al. 2012, MNRAS, 419, 687
Ramos Almeida, C., Tadhunter, C. N., Inskip, K. J., et al. 2011, MNRAS, 410, 1550
Rigby, J. R., Diamond-Stanic, A. M., & Aniano, G. 2009, ApJ, 700, 1878
Shi, Y., Rieke, G. H., Hines, D. C., et al. 2006, ApJ, 653, 127
Siebenmorgen, R., Haas, M., Kruegel, E., & Schulz, B. 2005, AN, 326, 556
Simpson, C. 1998, MNRAS, 297, L39
Singh, V., Shastri, P., & Risaliti, G. 2011, A&A, 533, A128
Smith, J. D. T., Draine, B. T., Dale, D. A., & Moustakas, J. 2007, ApJ, 656, 770
Smolčć, V., & Riechers, D. A. 2011, ApJ, 730, 64
Spoon, H. W. W., Marshall, J. A., Houck, J. R., et al. 2007, ApJL, 654, L49
Sturm, E., Hasinger, G., Lehmann, I., et al. 2006, ApJ, 642, 81
Sturm, E., Lutz, D., Verma, A., et al. 2002, A&A, 393, 821
Tadhunter, C., Dicken, D., Holt, J., et al. 2007, ApJL, 661, L13
Tadhunter, C., Dickson, R., Morganti, R., et al. 2002, MNRAS, 330, 977
Tadhunter, C., Holt, J., González Delgado, R., et al. 2011, MNRAS, 412, 960
Tadhunter, C. N., Morganti, R., di Serego-Alighieri, S., Fosbury, R. A. E., & Danziger, I. J. 1993, MNRAS, 263, 999
Tadhunter, C. N., Morganti, R., Robinson, A., et al. 1998, MNRAS, 298, 1035
Tadhunter, C. N., Ramos Almeida, C., Morganti, R., et al. 2012, MNRAS, 427, 1603
Urry, C. M., & Padovani, P. 1995, PASP, 107, 803
Veilleux, S., Rupke, D. S. N., Kim, D., et al. 2009, ApJS, 182, 628
Wall, J. V., & Peacock, J. A. 1985, MNRAS, 216, 173
Wills, K. A., Tadhunter, C. N., Robinson, T. G., & Morganti, R. 2002, MNRAS, 333, 211